Study of Bi_2O_3-RGO Nanocomposites as Electrode Materials for Energy Storage Nanodevices

By

Qudrat Ullah

Supervised by

Prof. Dr. Javed Iqbal Saggu

Laboratory of Nanoscience and Technology (LNT)

Department of Physics

Quaid-i-Azam University Islamabad Pakistan

Session 2021-2023

“In the name of ALLAH, the Most Gracious, the Most Merciful”

Study of Bi_2O_3-RGO Nanocomposites as Electrode Materials for Energy Storage Nanodevices

By

Qudrat Ullah

Supervised by

Prof. Dr. Javed Iqbal Saggu

Laboratory of Nanoscience and Technology (LNT)

Department of Physics

Quaid-i-Azam University Islamabad Pakistan

Session 2021-2023

This work is submitted as a dissertation in partial fulfillment

of the requirement for the degree of

MASTER OF PHILOSOPHY

IN

PHYSICS

To The

Department of Physics

Quid-i-Azam University Islamabad, Pakistan (2023)

CERTIFICATE

The research work reported in this thesis is entitled **"Study of Bi_2O_3-RGO Nanocomposites as Electrode Materials for Energy Storage Nanodevices"** by **Qudrat Ullah**, Reg. No.**02182113013,** Session **2019-2023,** submitted to Quaid-i-Azam University Islamabad for the degree of Master of Philosophy (M.Phil) in Physics is a record of bonafide research carried out by him in the Laboratory of Nanoscience and Technology (LNT), Department of Physics under my supervision. I believe that this thesis fulfils part of the requirement for the award of the degree of Master of Philosophy. The results embodied in the thesis have not been submitted for the award of any other degree.

Chairman:

Prof. Dr. Kashif Sabeeh

Department of Physics,

Quaid-i-Azam University Islamabad, Pakistan.

Supervisor:

Prof. Dr. Javed Iqbal Saggu

Department of Physics,

Quaid-i-Azam University Islamabad, Pakistan.

DEDICATION

This thesis is dedicated to my

MOM

(Adil Bi Bi)

ACKNOWLEDGMENTS

First and foremost, I am grateful to **Almighty ALLAH** for His countless blessings that enabled me to contribute constructive research work for the welfare of humanity, as the Holy Quran instructs Muslims to "contemplate the wonders of creation" (Quran 3:191). Muslims are encouraged to seek knowledge, explore the universe, and find the "Signs of Allah" in His creation. Along with this, thousands of blessings upon **Prophet Muhammad (S.A.W),** an ideal source of guidance for humanity and a role model for humans.

I want to thank my supervisor, **Dr. Javed Iqbal Saggu,** for his invaluable cooperation and unwavering motivation throughout the research work. His guidance and support have been instrumental in shaping the success of this endeavor. I am truly fortunate to have such a dedicated and inspiring mentor and supervisor by my side.

My mother has been the sincerest and supportive individual (**Adil Bi Bi Marwat**). She has been my constant pillar, providing financial assistance and unwavering motivation to strive for a better future. Equally, my father (**Muhammad Khan Betani**) holds the utmost respect in my life, profoundly impacting me. The kindness, sacrifices, and hardships they endured on my behalf are immeasurable, and I know I will never be able to repay them in my lifetime. I also want to mention my brothers Rafi and Farid; they have supported and motivated me throughout my academic journey.

I will especially mention my classmates and secret partners **Muhammad Oneeb Ktk & Mehwish Parveen**, I will always miss their company. I am immensely thankful to laboratory mates **Dr. Asifa, Mr. Ahamad Niazii,** ex-senior **Ms. Amara Gandapoor, Ms. Rida,** and **Mr. Ameen, Mr. Hamza, Mr. Haider**, they are always cooperative. Their support and camaraderie throughout the two semesters made my time here truly enjoyable, and I will dearly miss their company. It would be an injustice If I did not mention my graduation teachers, **Dr. Tabasum Nasir, Dr. Hafeez Ullah, Dr. Saeed Ullah, Madam Rubina,** and **Rizwan Ullah**. I am deeply thankful for their invaluable contributions to my academic journey.

Qudrat Ullah Shahab

Contents

List of Figures

List of Tables

List of Abbreviations

Bi_2O_3	Bismuth Oxide
GNPs	Graphene Nanoplatelets
RGO	Reduced Graphene Oxide
EHDs	Energy Harvesting Devices
EESDs	Electric Energy Storage Devices
SCs	Supercapacitors
NCs	Nanocomposites
XRD	X-Ray Diffraction
ESR	Equivalent Series Resistance
LIBs	Lithium-ion Batteries
EDLCs	Electric Double Layer Capacitors
CV	Cyclic Voltammetry
GCD	Galvanostatic Charge-Discharge
EIS	Electrochemical Impedance Spectroscopy
NPs	Nanoparticles
FTIR	Fourier-transform infrared spectroscopy
SEM	Scanning Electron Microscopy

Abstract

In this study Bi_2O_3 nanoparticles have been synthesized via simple and versatile co-precipitation technique while Bi_2O_3/RGO NCs by in-situ approach with different ratios of RGO in host matrix, $(Bi_2O_3)_{0.75}/(RGO)_{0.25}$, $(Bi_2O_3)_{0.50}/(RGO)_{0.50}$ and $(Bi_2O_3)_{0.25}/(RGO)_{0.75}$. The fabricated NCs material successfully integrated the electrode performance with synergistic effects, contributed by Bi_2O_3 and RGO nanoparticles. The structural, vibrational, and optical properties were studied by X-ray diffraction (XRD), FTIR, and UV-visible spectroscopy techniques. The supercapacitor behavior was studied using cyclic voltammetry, galvanostatic charge-discharge, impedance analysis, cycle stability, and coulombic efficiency respectively. The NC electrode material $(Bi_2O_3)_{0.50}/(RGO)_{0.50}$ has achieved a superior specific capacitance of 1254.9 F g^{-1} at a scan rate 5 mV/sec in 6 M KOH electrolyte. Moreover, this electrode material has achieved an outstanding specific energy density of 27.92 Wh/Kg and a specific power density of 900 W/Kg with a cycle retention of 99 % over 1000 cycles, with low ohmic resistance of 1.255 Ω. The high specific capacitance, power density, and energy density with low ohmic resistance of the prepared nanocomposite is an excellent choice for energy storage devices with low voltage drop and minimal energy loss in the form of heat and with the long lifetime of the capacitor.

Chapter No.01 Introduction

1.1 Materials & Material Science

Materials are the essence of everything around to use daily, from our clothes to the devices. It is essential to comprehend how they behave at the atomic and molecular levels to design and produce materials with the appropriate qualities for particular applications. The scientists, engineers, and researchers of the respective field investigate the links between a material's composition, structure, processing techniques, and final qualities. This knowledge empowers us to design materials for various applications, including electronics, aerospace, medicine, and energy storage.

The study of solid material properties and how a material's composition changes certain features is known as Material Science. This scientific investigation is the result of a combination of solid-state since the wide variety of material qualities cannot be understood within the context of any one of the three specified classical disciplines: Physics, Metallurgy, and Chemistry are required. In today's science and technological era, Material Science is extremely important. Several materials are utilized in construction, industries, transportation, and other fields to suit the needs of the plant and the individual [1].

Based on its significance and applicability, the area of Material Science was first referred to as "Metallurgy" in 1960 [2]. Figure 1.1 provides the framework Material Science framework.

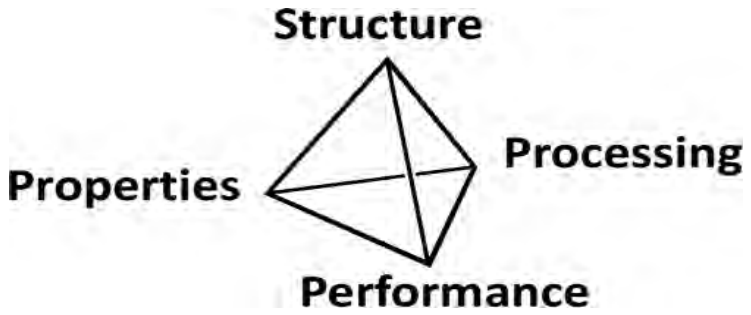

Figure 1. 1: Tetrahedron of the material in its usual shape [3]

Material Science investigates connections between the ingredients, their behavior, and the applications of materials. Generally, materials among structure can be thought of as its fundamental arrangement of atoms and molecules at the submicroscopic level. In contrast, a material's property is an attribute that relates to a particular response to an applied stimulus.

In the discipline of Material Science, there are four essential components, which are processing, structure, characteristics, and performance. The processing of a material determines its structure, but its ultimate performance is based on its attributes. Understanding how characteristics, processing, and structure interact choosing the suitable material with the characteristics needed for a particular application is essential. The expansion of available material kinds is another factor that has contributed to technological development in different stages [4].

1.2 Nanomaterials

The prefix "Nano" comes from the Greek word "dwarf," which implies "ultra-small", which is referred to as a nanometer or one billionth of a meter (10^{-9}m). This research is in nanoscience, which ranges from 1-100 nm in nanometer-scale structures and molecules. These materials are used in electronics and applications using nanotechnology [5]. Nanoscience can modify the environment around us and might result in remarkable advancements in multiple industries, from production to medical services. Although the terms "Nano-Science" and "Nano-technology" are sometimes used synonymously, these concepts are different.

1.2.1 Nanoscience

The study of materials and structures on the incredibly small size (nanometer) and their characteristics, uses, and manipulation is all included in nanoscience (10^{-9}m scale). Nanoparticles are defined as particles with a size between 1 and 100 nm. The understanding of nanoscale structures, characteristics, and dimensions of materials is the focus of nanoscience [3]. It seeks to efficiently develop nanoscale structures and gadgets for use in daily life. The cross-disciplinary research is being done in various domains, including Physics, Chemistry, Biology, Computing, and Medicine, to better comprehend the world around us. Nanoscience focuses on understanding of materials' nanoscale structures, characteristics, and dimensions [6]. It seeks to efficiently develop nanoscale structures and gadgets for use in daily life.

1.2.2 Nanotechnology

Nanotechnology, often known as "molecular manufacturing," is the modelling and fabrication of devices at the nanoscale and using nanoscale systems and structures. Richard

Feynman's similar remark inspired the founding of nanotechnology, "There's plenty of room at the bottom," made in 1959 at an American Physical Society gathering. He also predicted that designing materials atom by atom through self-assembly would not violate any preexisting physical laws. Since Nori Taniguchi first coined the term "Nanotechnology" in 1974, a significant amount of study has been done on creating novel materials, their uses, and characterization methods for examining nanomaterials [7].

These days, investors, governments, and the business sector have high expectations for nanotechnology because it is receiving so much attention. Because of its extraordinary ability to build new structures at the atomic level, it has already developed in future industries produce innovative materials and devices with a diverse range of potential applications. Significant improvements in the energy sector are among them to keep up with our increasing energy thirst, which develops along with the population approaching the developed economies and our demand per capita. As more evidence of human impact on the environment comes to light, this needs to be done in a way that takes the environment into account when calculating wealth output [8].

1.3 Energy Storage

The rapid growing of population and their changing lifestyles due to the deficiency of natural resources, the production and storage of energy are now the most pressing issues that need to be addressed (e.g, fossil fuels, etc.). There are two main energy sources: regulated power plants, which include nuclear power plants, fossil fuels, geothermal power plants, and other are biofuel sources. In addition, there are non-dispatchable renewable energy resources such as solar, wind, and water-driven hydropower. People right now, or at least in the near future, cannot solely rely on renewable energy sources. A theoretical estimate of an ideal scenario states that renewable energy sources should meet 100% of the world's energy consumption, but this is not achievable. However, the proportion of renewable energy sources can be raised at the expense of more study and application. Figure 1.2 indicates the renewable energy forecasting according to the 2019 report of US Energy Information Administration (EIA).

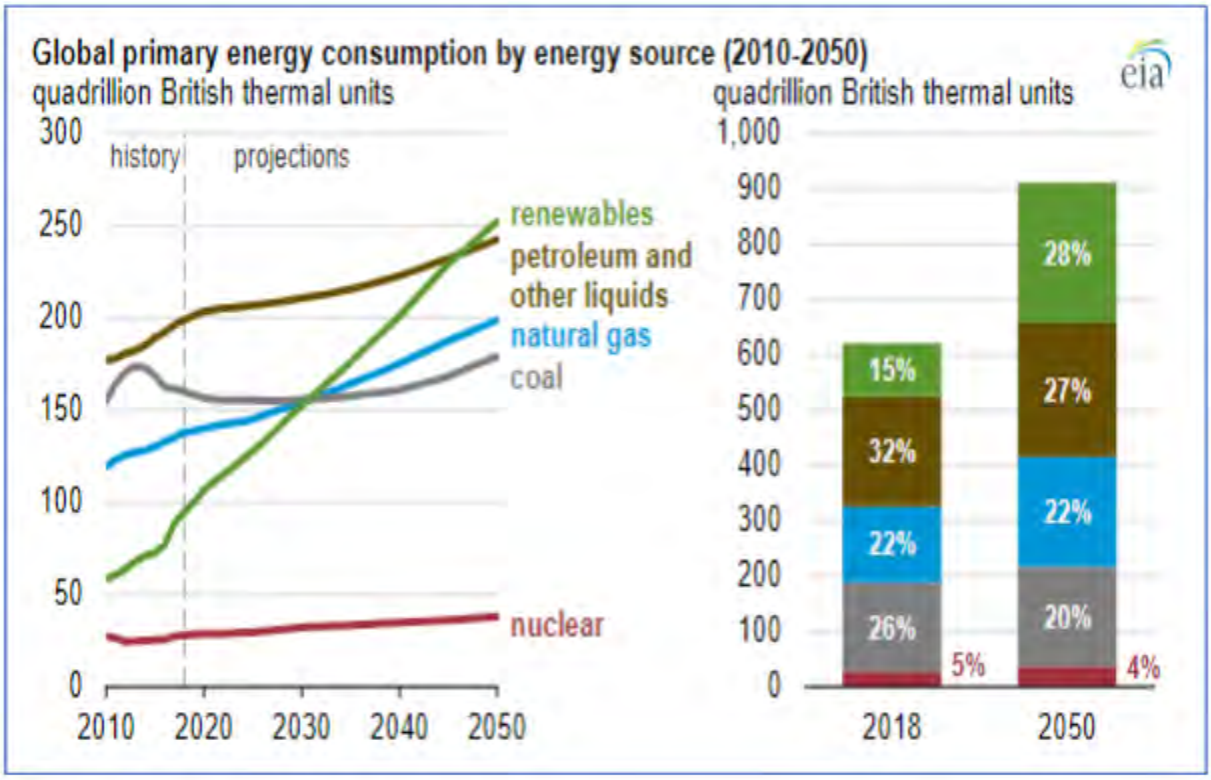

Figure 1. 2: The renewable energy forecasting according to the US EIA 2019 report [9]

1.4 Energy Storage Devices

The storage of energy produced from renewable sources and other alternatives is necessary for usage in the future and is currently a growing field of research for academics. There are a variety of ways to store energy, some of which include the use of batteries or specialized hydropower plants, as well as some other experimental options like the superconductive magnetic energy storage system (SMES), which stores energy in a magnetic field generated in a superconducting coil by the flow of electrical charges and by cooling it cryogenically below the critical temperature [10].

Some other energy storage systems are incompatible with regular energy storage systems because they are part of their ongoing phase of basic research. There are some parameters to keep in mind while considering energy production; one is to sustain a clean environment by reducing pollutants, i.e., by replacing combustion engines with electric vehicles. Batteries are used in electrical vehicles like Autonomy. Electric vehicles store electrical energy in batteries. The advanced technological development for storage purposes uses batteries, especially Li-Ion

batteries. In comparison, supercapacitor technology is a good alternative to conventional batteries used in electric vehicles. Supercapacitors or ultra-capacitors can store a good amount of electrical energy. The first SCs has first developed in the middle of the 20th century. Some United States companies like General Electric (GE) and Standard Oil of Ohio (SOHIO) have set up the first supercapacitor experiment. These electrochemical capacitors could show a capacity of about 1F. The "Gold Cap", the first supercapacitor of the time, was released by Panasonic Company in 1982 with a high ESR. From 1982 to 1992, many EDLCs were introduced with low ESR and could have a nominal capacity of up to 1kF. Currently, most supercapacitors have a capacity in the several thousand Farad range with a tenth-hundredths range of charge-discharge (CD) currents. The characteristic property of supercapacitors is that they can operate with extremely high currents compared to batteries. The comparison of power density as a function of energy density of various energy storage systems described in figure (1.3).

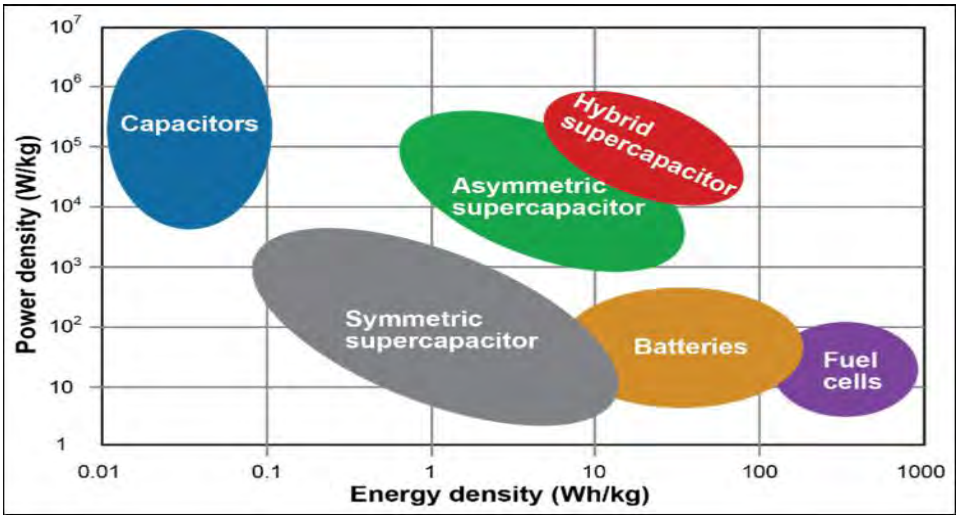

Figure 1. 3: Power density vs energy density for different energy storage devices [1]

Supercapacitors are defined by their ability to store and release a considerable amount of electrical energy in a short period. They are used in many applications, such as wind turbines, trains, trolleybuses, fuel cell vehicles, electric vehicles, and hybrid electric vehicles (HEVs), performing better than conventional batteries [11].

1.4.1 Renewable Energy Storage Devices

Further classification of renewable energy storage devices are,

- Energy Harvesting Devices (EHDs)
- Energy Storage Devices (ESDs)

1.4.1.1 Energy Harvesting Devices (EHDs)

The EHDs convert energy directly from its raw form into usable form. The two most often used EHDs are solar cells and electrochemical cells, which directly convert fuel into electricity and solar light energy [12]. Solar cells work on the principle of the photovoltaic effect, whereas electrochemical cells behave similarly to batteries with the exception that they cannot be recharged. among the several forms, hydrogen fuel cells are the most well-known. [13].

1.4.1.2 Energy Storage Devices (ESDs)

ESDs are further classified and described as under.

1.4.1.2.1 Non-Electrical ESDs

Kinetic and thermal energy are transformed into electrical energy by the non-electrical ESDs. The hydropower plants and flywheels are examples of non-electrical ESDs.

1.4.1.2.2 Electrical Energy Storage Devices (EESDS)

Well-known EESDs that transform electric, chemical, and magnetic energies into electricity include batteries, capacitors, inductors, and superconducting magnetic energy storage devices (SMES). These EESDs store energies in electric and magnetic devices before electricity Conversion [14]. Batteries, capacitors, and supercapacitors (SCs) can be categorized based on essential factors. Table 1.1 depicts some important statistics of these EESDs parameters. [15].

Table 1. 1 Comparison among the EESDs [16]

Characteristics	Lithium-ion Batteries	Liquid Supercapacitors	Conventional Solid Supercapacitors	Current FlashCharge Batteries
Specific energy	200 Wh/kg	30 Wh/kg	5 Wh/kg	30 Wh/kg
Energy density	230 Wh/L	40 Wh/L	10 Wh/L	60 Wh/L
Specific power	0.2 kW/kg	2 kW/kg	0.25 kW/kg	4 kW/kg
Power density	0.3 kW/L	3 kW/L	0.5 kW/L	8 kW/L
Cycle life	~1000	>50,000	>50,000	>50,000
Temperature window	0°C to 50°C	0°C to 50°C	-30°C to 80°C	-30°C to 80°C
Charge rate	-	Faster than Lithium-ion	Faster than Lithium-ion	20 times faster than Lithium-ion
Safety	Flammable/ toxic	Flammable/ corrosive/ toxic	Safe	Safe
Flexibility	Minimal	Minimal	High	High

1.5 Batteries

A battery is a device that holds electrical energy with a chemical foundation. It utilizes an electrochemical method to convert stored chemical energy into direct (DC) electrical energy. The electrochemical process in a battery occurs when electrons are transferred through an electric current from one substance (referred to as the electrodes) to another. In 1800, Italian physicist Alessandro Volta invented the first battery.

Batteries are often used as electrochemical energy storage devices (EESDs). Batteries stand out among the well-known EESDs due to their unique characteristics, such as cyclic charging-discharging, portability, ease of use, and wide range of power storage (100 watts to 20 Mega Watt). Chemical reaction activation in each battery cell and subsequent conversion of chemical energy to electrical energy make up batteries' charging and discharging operation. Among the numerous types of batteries utilized (NiCd) are Lead Acid Batteries (LAB), Nickel-Metal Hydride (NiMH) Batteries, Lithium-Ion Batteries (LIBs), Sodium-Ion Batteries (NIB/SIB), Nickel-Zinc Batteries, and Nickel-Cadmium Batteries. Because they can function at high voltages, have low self-

discharge rates, and have better energy densities than other battery choices, Ni-Cd and LIB batteries are two of the most widely used battery kinds. Over the past ten years, batteries have proven to be a substantial energy source. Additionally, batteries can be found in various sizes and varieties depending on the user's needs. Several different kinds of batteries are described below and shown in figure 1.4;

- Lead-Acid batteries(LAB)
- Nickel-Cadmium Batteries (Ni-Cd)
- Nickel-metal hybrid Batteries (Ni-MH)
- Lithium-ion Batteries (Li-ion)
- Alkaline Batteries(AB)
- Zinc-carbon Batteries(ZCB)
- Coin cell Batteries(CCB)
- Zinc-air cells(ZAC)
- Sealed lead-acid Batteries(SLB)

Figure 1. 4: Different types of batteries [17]

1.7 Supercapacitors

Supercapacitors are promising candidates for powerful devices. These strong devices are anticipated to have many applications in different modern technologies. When supercapacitors' energy and power densities are maximized, their significance becomes clear. The primary research focuses on the electrode material, fabrication, alteration of the electrode material, and electrolyte to accomplish these supercapacitors' essential characteristics and performance. Supercapacitors, also known as electrochemical or ultra-capacitors, it consists of very thin layers of dielectric and a large surface area electrode specifically. Their surface area can be increased with the help of carbonaceous material. Consequently, these supercapacitors have their specific capacitance many orders of the traditional capacitors. Supercapacitors are utilized, individually or in collaboration with fuel cells or batteries, for many energy storage applications. The enormous number of charge-discharge cycles, high power potential, and robust thermal operating range of supercapacitors are attractive characteristics compared to conventional energy storage devices. Supercapacitors have a larger energy storage capacity and a higher power supply rate than rechargeable batteries. Supercapacitors' energy densities, however, are lower than those of fuel cells and batteries. For applications that rely on an energy supply for a considerable amount of time, this demands a combination of batteries and other power supply resources. The improvement in SC's energy density, comparison to batteries, is the emerging goal of the researchers.

- Compared to a typical capacitor, its plates have a large surface area.
- The separation between the plates in SCs is relatively narrow because the separator functions differently than a traditional dielectric.
- In contrast to a regular capacitor, which uses a solid or dry substance as a dielectric medium, a supercapacitor uses a liquid or wet electrolyte between its electrodes.

A supercapacitor is made up of two metallic plates (electrodes), which are connected ionically and are spaced apart by a separator and an “electrolyte" (a material dissolved in a polar solvent, such as water). The porous material, typically carbonaceous materials, is placed on the metallic "electrodes," increasing the electrodes' surface area for charge storage. The porous structure of the plates acts like a sponge that absorbs electricity and it is shown in figure (1.5).

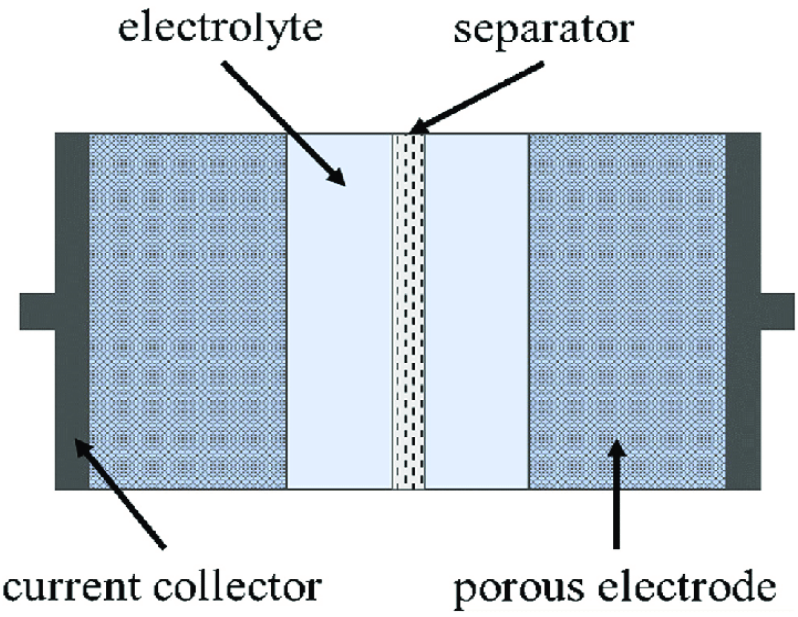

Figure 1. 5: The schematic diagram of a supercapacitor [1]

Potential applied polarized ions in the electrolyte are separated from the capacitor electrodes and create electric double layers that are one ion in size. At the interface of each electrode, there is an opposing ionic charge layer and a balancing charge layer. The ions from the double layer are likely to be adsorbed by the electrode surface area, resulting in the pseudocapacitive phenomena. The kind of electrode material and its surface area frequently encourage this phenomenon. The basic structure of conventional capacitors governs the capacitance" of supercapacitors and can calculated by using the equation (1.5).

$$C = \epsilon_o \epsilon_r \, A/d \qquad (1.1)$$

Where "ϵ_0" shows free space permittivity, relative permittivity is indicated by "ϵ_r" while "A" represents the plate's surface area, and the distance between two oppositely charged electrodes is represented by **"d"**. The two electrodes' capacitors, C_1 and C_2 form a series two circuit where the new capacitance C_{total} of the capacitor can b estimated with the following.

$$C_t = \frac{C1.C2}{(C1 + C2)} \qquad (1.2)$$

Supercapacitor electrodes may have symmetric or asymmetric geometry, where symmetry indicates that two electrodes have comparable capacitance values, resulting in a net capacitance equal to half that of a "single" electrode.

$$C_t = 1/\ 2\ C_1 \qquad \text{if } "C_1 = C_2" \qquad (1.3)$$

On the other hand, the net capacitance is equal to a lesser capacitance value in the case of an asymmetric capacitor.

$$Ctotal \approx C_2 \qquad \text{if } C_1 \gg C_2 \qquad (1.4)$$

The mathematical formula for a capacitor's capacitance per unit of active mass is as follows.

$$C_s = \frac{I \nabla t}{\nabla V.m}\ [Fg^{-1}] \qquad (1.5)$$

Where **"m"** represents the active material of the electrode, **"Q"** and **"ΔV"** represent the average charge on the electrodes and potential window, respectively.

1.7.1 Types of Supercapacitors

Supercapacitors are divided into three categories: Electrochemical Double Layer Capacitors (EDLC), Pseudocapacitors, and Hybrid Capacitors. As their names indicate, the third category comprises an EDLC and a Pseudocapacitors combination.

Supercapacitors Classification:

- Electrostatic double-layer capacitors
- Pseudo capacitors
- Hybrid capacitors

1.7.1.1 Electrostatic Double Layer Capacitors (EDLC)

Supercapacitors, also known as electrostatic double-layer capacitors (EDLC), work based on electrostatic charge separation. These devices use an electrode material with a high surface area, like activated carbon, to provide a large interface for charge buildup. When a voltage is applied, ions from the electrolyte build up at the electrode-electrolyte interface, creating a double layer with apparent charge separation. With the help of this process, EDLCs may store electrical energy free of chemical reactions, leading to quick charge and discharge cycles [18].

Due to their exceptional qualities, EDLCs are used in many different industries. EDLCs outperform other supercapacitor types, including Pseudocapacitors, in terms of high-power density and long cycle life. Pseudocapacitors use faradaic redox processes to store energy, enabling larger energy densities but frequently at the expense of worse cycle performance. In contrast, EDLCs

give up energy density in exchange for superior power output and cycling endurance [19]. The capacitance of EDLCs can be calculated with the same formulation as for the traditional capacitors.

$$C = \epsilon_o \epsilon_r \frac{Ae}{d} \qquad (1.6)$$

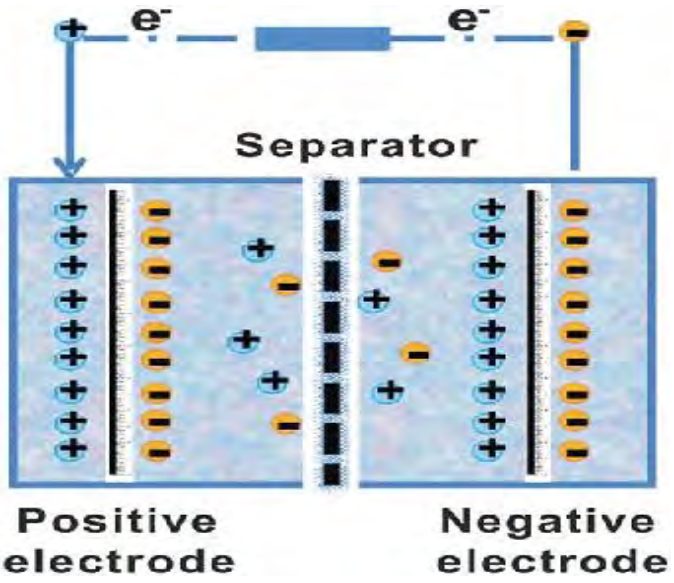

Figure 1. 6: Schematic representation of EDLC-type supercapacitor [1]

Where "d" is the thickness of the double layer formed. As the capacitance and energy of the capacitors varies inversely with the value of "d", so as a result great amount of energy can be stored in these capacitors. Figure 1.6 depicts the schematic representation of EDLC-type SC.

Application areas for EDLCs include electronics (by providing peak power to gadgets), transportation (regenerative braking in automobiles), renewable energy (buffering energy from solar/wind sources), and even medical devices (delivering high-energy pulses). The energy density of other supercapacitor types may be higher, but EDLCs are still superior regarding quick energy delivery and long operating life. As research develops, supercapacitor design optimization may synergize strengths, creating new opportunities for energy storage solutions in various industries.

1.7.1.2 Pseudocapacitors

Pseudocapacitors are also known as electrochemical pseudocapacitors where, in contrast to EDLCs, the method for storing energy is based on the oxidation-reduction (Redox) reactions, electrosorption and intercalation mechanism, involving electrode materials of high energy oxides", carbons doped with metal or conducting "polymers [20]. Because of the faradic processes, a

pseudocapacitors has higher "C_s" and "E_g" than EDLCs. Pseudocapacitors rely on "de-solvated" and absorbed ions to cause electronic charge transfer between the electrode and electrolyte [21]. Figure (1.7) represents Pseudocapacitor diagram.

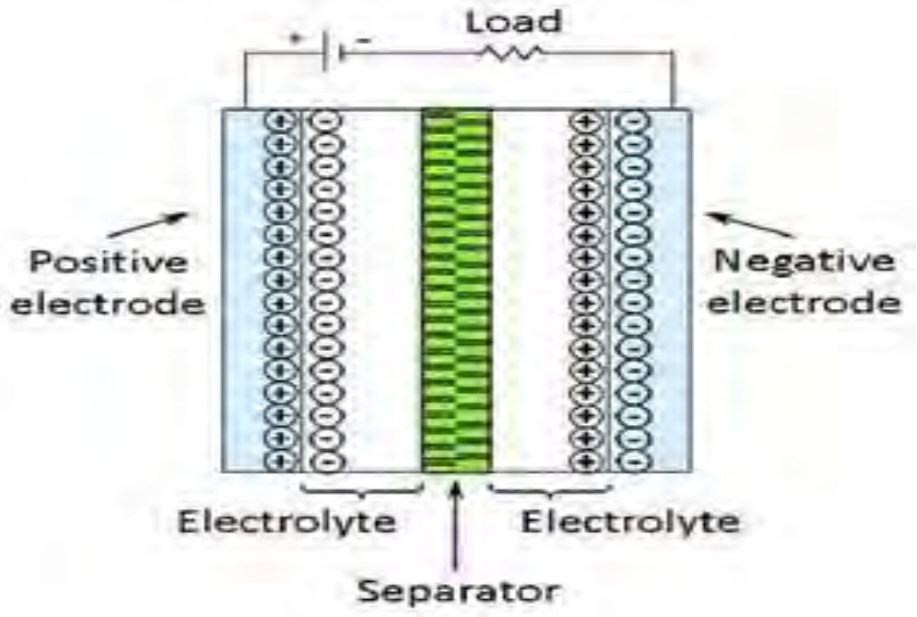

Figure 1. 7: Schematic representation of pseudo-type supercapacitor [22]

In this mechanism, only transfer of charge occurs because of no interaction between Adsorbed ions and the material atoms. For electrodes to reach pseudocapacitance capacity depends Upon the material's "chemical affinity" to the ions absorbed on the electrode surface. Achievement this effect is also linked with the structural and dimensional geometry of the pores (electrode). In Pseudocapacitor, the storage of charges increases linearly with applied voltage. Materials used in pseudocapacitors as electrode material exhibit redox behavior and these materials include metal oxides SnO_2, Zno, Bi_2O_3, PbO, Sb_2O_3, transition metal oxides (TMOs), such as CO_3O_4, V_2O_5, NiO, MnO_2, Fe_3O_4, RuO_2, transition metal sulfides and conducting polymers such as poly-phenylene-vinylene (PPV), poly (4-styrene sulfonate) (PSS), Polyaniline (PANI), Polypyrrole (PPY), Polythiophene and Polyacetylene etc.

1.7.1.3 Hybrid Capacitors

The hybrid capacitors, as the name indicates must possess the characteristics of two capacitors i.e, EDLC and Pseudocapacitors. In its components, the electrodes possessing different properties are used, i.e, one electrode with electrostatic capacitance and the other with electrochemical capacitance. Lithium-ion capacitor is an example of such Hybrid Capacitor.

1.8 Metal Oxides

A metal oxide is a chemical compound that is formed when a metal reacts with oxygen. Metal oxides are commonly found in nature as minerals, and they are also frequently produced as a byproduct of various industrial processes. There are many different types of metal oxides, and they can be classified according to the metal that they contain. Some examples of common metal oxides include aluminum oxide, iron oxide, and copper oxide. The properties of a metal oxide depend on the type of metal it contains, as well as the oxidation state of the metal. Figure 1.8 shows application of SCs in various industries.

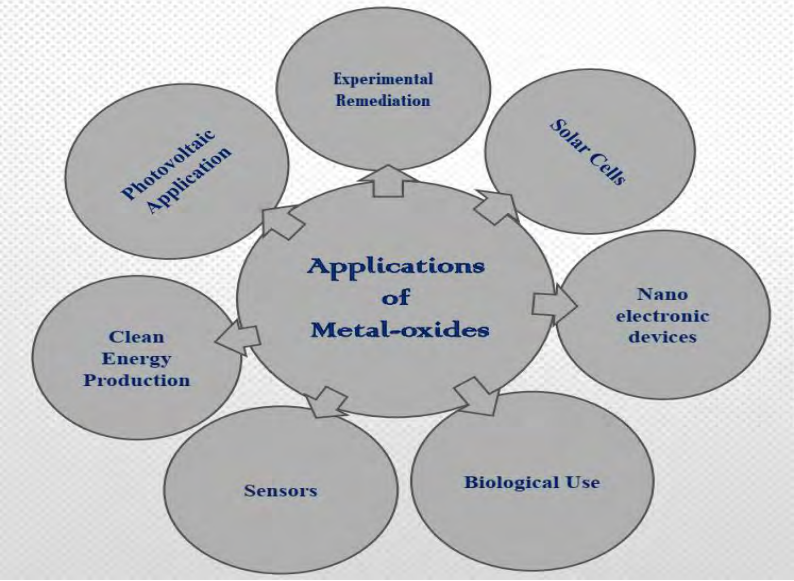

Figure 1. 8: Applications of metal oxides [1]

One of the most important properties of metal oxides is their reactivity. Many metal oxides are highly reactive, and they can easily react with other chemicals to form new compounds. For example, aluminum oxide is a very reactive substance that can react with water to form aluminum hydroxide. Iron oxide, on the other hand, is a less reactive substance and typically does not react with water. The reactivity of metal oxides is often related to their ability to act as catalysts. A catalyst is a substance that can speed up a chemical reaction without being consumed in the process. Many metal oxides are excellent catalysts and can be used in a variety of industrial processes to speed up chemical reactions.

In addition to their reactivity, metal oxides also have other important properties. For example, some metal oxides are good electrical conductors, while others are poor conductors. Some metal oxides are also good insulators, which means that they are not good at conducting

electricity. The physical properties of metal oxides also vary widely. Some metal oxides are solid at room temperature, while others are liquid or gas. The density of metal oxides can also vary significantly, with some being very dense and others being relatively light. Overall, metal oxides are a diverse and important class of chemical compounds. They are found in many different forms and have a wide range of properties, making them useful in a variety of applications.

1.8.1 Bismuth Oxide

Bismuth Oxide (Bi_2O_3) is a chemical compound that consists of bismuth and oxygen atoms. It is a white, crystalline solid that is typically found in occurs naturally in the earth's crust as the mineral bismite. Ceramics, Pigments, and Pharmaceuticals are just a few of the many industries that use Bismuth Oxide. Bismuth oxide has been investigated as a viable material used in supercapacitors as electrode components in the field of energy storage.

Supercapacitors are energy storage devices that can instantly deliver enormous amounts of power and have a variety of possible uses, such as in small electronics and electric vehicles. One of the key properties of bismuth oxide that makes it attractive for use in supercapacitors is its high surface area to volume ratio, which allows it to store a large amount of charge. In addition, bismuth oxide has a high dielectric constant, which means that it can store a large amount of electrical charge in a small volume. However, there are several challenges to using bismuth oxide in supercapacitors. For example, it is a relatively poor conductor of electricity, which can limit its ability to deliver power quickly. Additionally, Bismuth Oxide is highly sensitive to humidity, which can affect its performance over time.

Despite these challenges, research on the use of Bismuth Oxide in supercapacitors is ongoing, and it is an active area of study. Scientists are working to develop new methods for synthesizing Bismuth Oxide and improving its performance to make it a more viable material for use in supercapacitors and other energy storage devices. Figure 1.9 shows arrangement of atoms in Bismuth Oxide molecules.

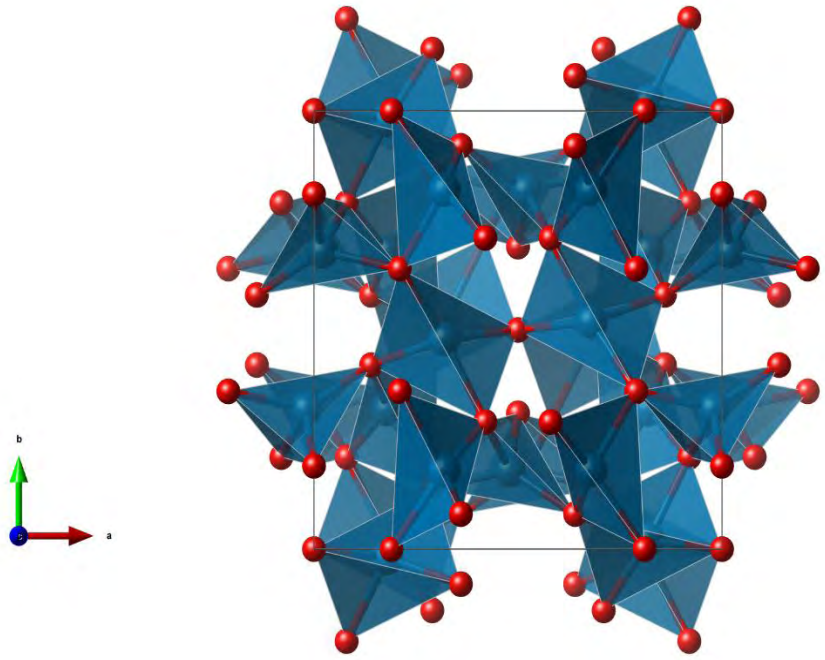

Figure 1. 9: Arrangement of atoms in Bi_2O_3 molecules

1.9 Carbon Derivatives

Carbon is the sixth element of the periodic table with an atomic number of six. Carbon is abundant in nature, and it plays a vital due to its capability to make complicated long chains of C-C bonding which specifically act as a ground for organic chemistry. Carbon's ability for unique chaining leads to the formation of countless compounds with fascinating properties. Different atomic arrangement and bonding changes the physical and chemical properties of carbon consequently. Carbon has acquired the great attention of researchers due to its unique allotropic forms, case of access, cost-effectiveness, eco-friendly nature, excellent conductivity, and high thermal stability [23]. Carbon material exists in different compositions and dimensionalities, which are unique to each other. The most known allotrope of carbon is Fullerene "0-D" and "1-D". Carbon Nanotubes (CNTs), Graphene (2-D), Graphite (3-D), and Diamond. The crystal structure of the above-mentioned allotropes is depicted in the following figure 1.10.

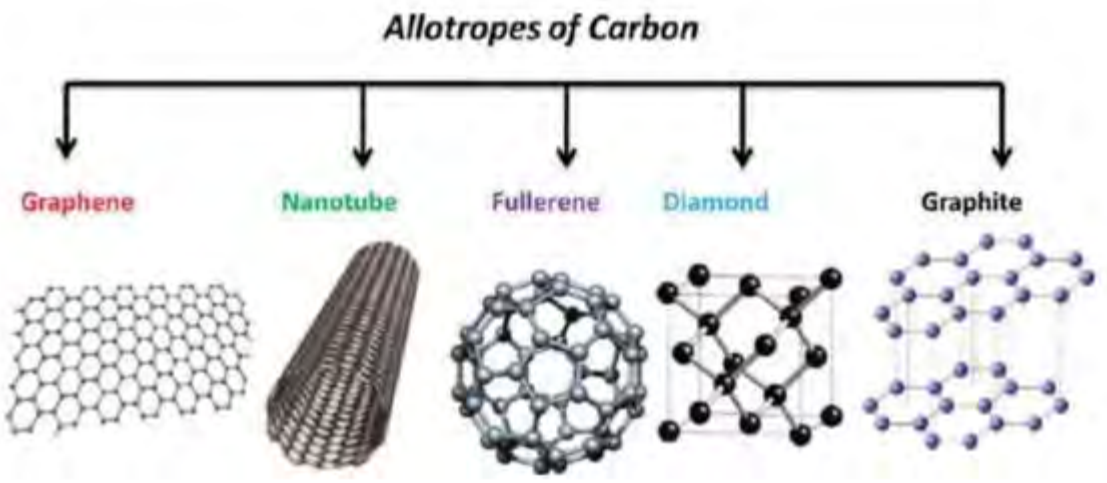

Figure 1. 10: The generation of synthetic carbon allotropes [24]

Carbon forms the toughest material like Diamond and the softest material like Graphite due to its the unique ability of bonding and hybridization. The strength difference from toughest to softest is attributed to bonding and hybridization. In the case of the toughest material Diamond sp_2 hybridization is responsible for its particular property toughness with tetrahedral structure and four δ-bonds having an angle of 109.5º whereas Graphite with its sp_3 hybridization has a trigonal structure and three δ-bonds at an angle of 120º [25]. Carbon-based materials are the key materials in advance applications of electronics, energy storage devices, solar cells, as an electrode material in SCs, photocatalysis and Li-ion batteries.

1.9.1 Fullerene

The next carbon allotrope after Graphite (3-D) and Diamond is called Fullerene, which was invented by H.W. Kroto and his colleagues in 1985. Different numbers of hexagons in this allotrope of carbon forms different molecules of fullerene in which highly symmetric molecule is C60, containing 60 atoms of carbon and has 20 hexagons and 12 pentagons in a cage-like structure. Usually, Fullerenes are used as a catalyst and ball bearings for lubrication and drug delivery devices [26].

1.9.2 Carbon Nanotubes (CNTs)

This carbon allotrope has a long and hollow structure with a slight wall thickness of carbon. sheets. CNTs are in the form of closed cages with honeycomb structures and large length-to-diameter ratio. This particular type of carbon is rolled into sheets with certain angles and diameters.

The different angles and diameters adopt the properties of nanotubes. In 1991, Iijima observed the multi-walled carbon Nanotubes (MWNTs), which consist of more than one layer of graphene, rolled into a tubular structure with pi-stacking, van der Wall forces, about 0.34 nm layer Separation, length of 1-100 microns with inner and outer radii 1-3 mm, 2-20 mm respectively. Later, in 1993, "Single-Walled Carbon Nanotubes (SWCNTs)" were observed by Bethune and Iijima. SWCNTs consist of a single layer of graphene with a few μm length and diameter in a range Of a few nm to 3 mm. The two parameters (n, m) define the structure of SWCNTs, representing. Chirality and twist of CNTs, respectively. The classification of SWCNTs can be based on the values of n, m parameters, i.e, chiral (n, m), Zig Zag (m, 0), and Armchair (n=m). These all are symmetric. Along their axis. The different and exclusive structures of CNTs have unique properties as high surface area, maximum stability, high conductivity, and strength with promising applications in Nano-electronics and chemical sensors [27].

1.9.3 Graphite

Carbon, being a polymorphic material exists in three forms, namely Diamond, Graphite and Fullerene. The carbon hybridization type differentiates graphite from diamond in a manner such that sp^3 (tetrahedral) hybridization of carbon bonding refers to the crystal structure Of diamond, whereas sp^2 (trigonal) hybridization of carbon bonds refers to the crystal structure of graphite. Consequently, diamond has a 3-D crystal structure, whereas carbon layers with covalent. and metallic bonding constitutes the crystal structure of graphite. These carbon layers are stacked in AB sequence and are linked through weak Vander wall forces originated by delocalized π-orbitals [28]. These carbon layers are called graphite layers. Being an anisotropic material, graphite is a good conductor of electricity and heat within its layers due to "metallic bonding" within the plane. On the other hand, it is a poor conductor of heat and electricity with reference normal to the layers due to weak van der Waal forces. This allotrope of carbon has both hexagonal and rhombohedral structure with different stacking layers, further affecting its properties [29]. ABCABC stacking of rhombohedral structure changes to ABAB stacking of hexagonal crystal structure due to its instability from lower to higher temperatures, respectively. Graphite has high conductivity, around 3000 W/mK, having a melting point of 4200K, and at high temperatures, the mobility of its electrons is about 30,000 cm^2/s. Graphite is widely used in various environmental, chemical and structural applications, and most commonly, it is used in electrochemical applications for energy storage purposes due to its porous nature. Mitra et al reported an increase

in specific capacitance, short response time, and long life of capacitors having graphite as an electrode material [30].

1.9.4 Graphene

The name “Graphene” is derived from the word “Graphite”. The suffix–end reflects the the fact that this carbon allotrope has so many double bonds. Graphene is a single-layered renowned allotrope of carbon atoms with two-dimensional (2D) atomic arrangement. It has hexagonal honeycomb lattice structure. Figure (1.11) shows arrangement of atoms in graphene.

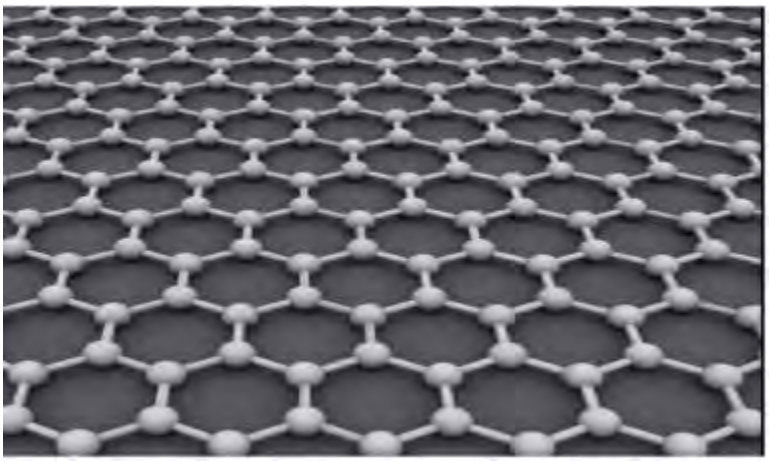

Figure 1. 11: Honeycomb hexagonal lattice “structure” of graphene [31]

Every single carbon atom in a graphene sheet is bound to its nearest three neighbor atoms, Via strong δ-bond. In graphene, the valence band is touched by the conduction band, which consequently makes, graphene is a semimetal with good electronic properties [32].

1.9.4.1 Properties of Graphene

The basic properties of Graphene are shown in Table (1.2).

Table 1.2: Theoretical properties of Graphene

Chemical name	Graphene
Appearance	Darkish Grey
Crystal Structure	2D, Hexagonal
Bandgap	Zero-Overlap semi-metal
Surface area	-2600 $m^2 g^{-1}$
Thermal conductivity	5000 Wm K-1
Charge carrier mobility	~250000 $cm^2 V^{-1}s^{-1}$
Mechanical strength	~1 Tpa
Resistivity	6×10^{-6} Ωcm^{-2}
Density	0.77 mg cm^{-2}
Interacting forces	Van der waal forces
Interatomic distance	1.42 Å
Interlayer distance	3.37 Å

1.9.4.2 Basic Graphene Structure

Carbon is the sixth periodic table element with six electrons and six protons "$^{6}C_{12}$". Electronic configuration of carbon is $1S_2$, $2S_2$, $2P_2$ ($2P_{1x}$, $2P_{1y}$, $2P_{0z}$), since "P" orbital has three sub orbitals, i.e. P_x, P_y, P_z, so $2P_2$ are arranged in such a way that $2P_z$ orbital is kept with no electron, though energy levels of $2P_x$, $2P_y$, $2P_z$ are equivalent. These valence electrons can form three types of hybridization (i.e. sp, sp^2, sp^3), namely Acetylene, Ethyl, and Methane forming geometry as linear, trigonal planar, and tetrahedral respectively [33].

1.9.5 Graphene Nano Platelets (GNPs)

Graphene is a revolutionary material of the 21st century and has great significance among Various allotropes of carbon due to its promising properties. The synthesis of graphene is comparatively complex and cannot be mass-produced yet, so alternatively, graphene nano-platelets (GNPs) are now widely used. Unlike graphene, which is a monolayer of graphene, The GNPs consist of a few graphite layers, varying in thickness (0.7 – 100 nm) [34]. Mostly, GNPs are synthesized by exfoliation of graphite up to 10-20 atomic layers. Along with its low cost and facile

manufacture GNPs are lightweight, have a high aspect ratio with a planar shape, and have excellent electrical and thermal conductivity and mechanical good [35]. GNPs have numerous applications as a neat coating, as compatible fillers, used as isolated material.

1.9.6 Reduced Graphene Oxide (RGO)

Reduced graphene oxide (RGO) has attracted a lot of attention recently due to its excellent qualities and many uses, especially in energy storage technologies like supercapacitors and batteries. The speedy electron transport is made possible by RGO due to its excellent electrical conductivity, allowing for quick charging and discharging cycles. This characteristic is essential for applications that require short bursts of energy, including grid stability in renewable energy systems or regenerative braking systems in electric vehicles. Additionally, their large specific surface area offers abundant locations for charge retention, which helps improve energy storage capacity and reliability.

RGO is suitable for long-lasting supercapacitor devices because of their mechanical resilience, which maintains their ability to endure across repeated charge-discharge cycles. Due to the exceptional electrochemical stability, which enables a wide working voltage window, RGO has higher energy and power densities. Additionally, RGO is compatible with various electrolytes, enabling them to be adapted to various supercapacitor designs and specifications. Further highlighting its versatility is the ability of RGO-based supercapacitors to use electric double-layer capacitance and pseudo capacitance, enabling a balanced approach to energy storage. As a result, very effective supercapacitors constructed of reduced graphene oxide are being developed, which may alter how energy storage is carried out in a variety of industries.

Chapter No. 02 Materials & Synthesis Techniques

2.1 Introduction

In disciplines such as energy storage devices, solar cells, photocatalysis, and medical science, nanomaterials have substantially affected our daily lives since last century. That is why it is crucial to understand the synthesis method of nanomaterials due to their various applications. So, this chapter deals with the synthesis of nanomaterials and nanocomposites and its fabrication. Today, advances in nanotechnology have introduced various techniques to synthesize and fabricate nanoparticles (NPs) from multiple materials. Since the size of the nanoparticles lies between 1-100 nm, its not that easy to manipulate atom by atom and molecule by molecule to get some desired shapes. The different synthesis approaches for nanomaterials are shown in figure (2.1). The size, shape, and geometry greatly influence nanomaterials' properties. Several methodologies and approaches have been reported to synthesize nanomaterials, out of which the two approaches that commonly used are;

1. Top-down approach
2. Bottom-up approach

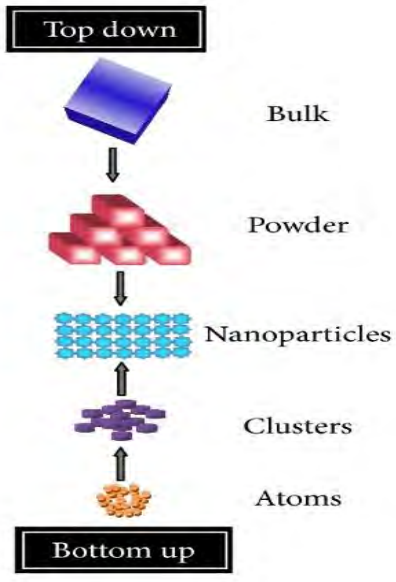

Figure 2.1: Different synthesis approaches for nanomaterials [36]

2.2 Top-down Approach

The top-down approach is a widely used strategy for the synthesis of nanoparticles in material science. The primary idea behind this approach is to break down a bulk material into smaller fragments until they reach the nanoscale regime. Several techniques are employed for the top-down synthesis of nanoparticles, including mechanical milling, laser ablation, and etching.

2.2.1 Ball Milling

It is a top-down approach that is used to synthesize the nanoparticles. The mechanical milling is a popular method that uses a high-energy ball mill to grind the bulk material into fine particles. The milling process generates high energy, which leads to breaking chemical bonds and creating nanoscale particles. Laser ablation is another technique where a high-intensity laser is focused on the bulk material, which generates a plasma plume. The plasma plume contains nanoparticles that can be collected and purified for further use.

2.2.2 Laser Ablation

Laser Ablation is an approach in which high-energy laser pulses vaporize a target material, typically a solid or liquid, to produce a plume of atoms or molecules. This plume can then be deposited on a substrate to synthesize nanomaterials with controlled properties. Laser ablation is a versatile and effective technique for synthesizing nanomaterials with controlled properties. It allows for the precise control of particle size, shape, and composition, which are critical factors in tuning the properties of nanomaterials. Following steps are used Here is a for laser ablation process for the synthesis of nanomaterials.

- Laser setup**:** A high-energy laser source is required to generate energy to vaporize the target material. The laser wavelength and pulse duration can be adjusted to optimize the ablation process and the properties of the resulting nanomaterials.
- Target material selection**:** The target material should be chosen based on the desired properties of the resulting nanomaterials. The common materials used for laser ablation include metals, metal oxides, and carbon-based materials.
- Ablation process: The laser pulse is focused on the surface of the target material, causing it to vaporize and form a plume of atoms or molecules. The plume expands rapidly, and the expelled species have the potential to cool and condense again to form nanoparticles. Particle collection**:** The nanoparticles generated in the plume can be collected on a substrate

placed in the plume's path. The substrate can be a solid material or a liquid, and the choice of substrate can affect the properties of the resulting nanomaterials.

The as-synthesized nanomaterials can be used in various applications, including energy storage, catalysis, sensors, and biomedical applications. Figure 2.2 explain the Laser Ablation process.

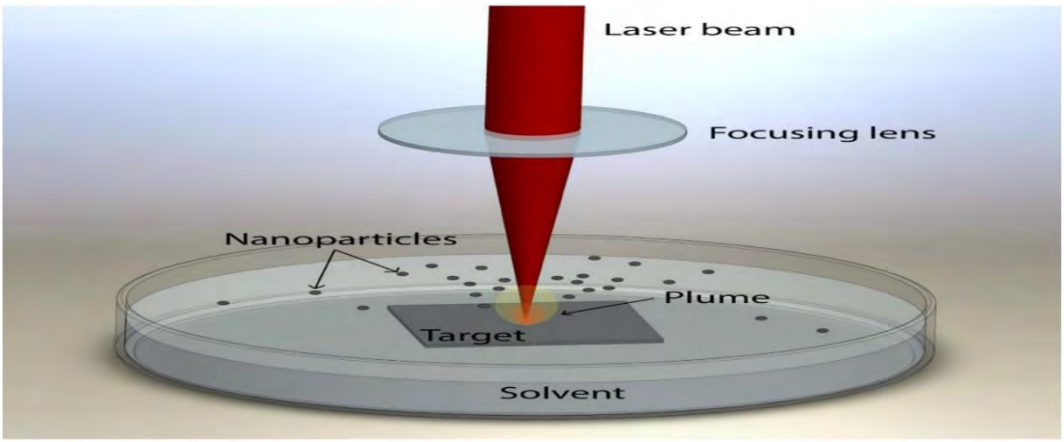

Figure 2. 2: Laser Ablation process [37]

2.2.3 Etching

Etching is a widely used method for the synthesis of nanomaterials, in which material is selectively removed from the surface of a solid to create a desired shape or structure. An appropriate starting material, such as a metal, metal oxide, or semiconductor, is chosen, and an etchant is applied, typically in liquid form. In order to produce the required shape and size of the nanomaterial, the etching rate is carefully managed by altering variables including temperature, pH, and etchant concentration. Once the desired dimensions are reached, the etching is stopped to prevent further material degradation, and the nanomaterial is washed to remove any residual etchant and then dried. Finally, the nanomaterial is characterized using various techniques such as electron microscopy, X-ray diffraction, and spectroscopy to confirm its desired properties. Etching is a versatile, cost-effective, and simple method for synthesizing nanomaterials with unique shapes and structures. However, controlling the etching process to achieve precise nanoscale dimensions can be challenging.

The top-down approach is a powerful strategy for the synthesis of nanoparticles in material science. The top-down approach has several advantages over other methods, including controlling

particle size, shape, and distribution. The various techniques used in the top-down approach offer distinct advantages, making it a versatile and useful method for the fabrication of nanoparticles. It also allows the creation of nanoparticles from a wide range of materials, including metals, oxides, and semiconductors.

2.3 Bottom-up Approach

The bottom-up approach for synthesizing nanoparticles in Material Science involves the assembly of atoms or molecules into nanoparticles through controlled chemical reactions. This approach allows for the precise control of nanoparticle size, shape, and composition, resulting in nanoparticles with unique and desirable properties. The process typically begins with selecting a precursor material, which is then reduced or oxidized in a controlled manner to form the desired nanoparticles. The process can be further refined by controlling the reaction conditions, such as temperature, pressure, and the addition of stabilizing agents. The bottom-up approach is widely used in the development of new materials with a range of applications, including catalysis, biomedical imaging, and energy storage.

Bottom-up approaches are techniques for producing nanoparticles that involve building materials from atomic or molecular components upwards rather than breaking down larger structures. Several techniques are used in bottom-up approaches to create nanoparticles, some of which are described here in detail.

2.3.1 Sol-Gel Synthesis Technique

The Sol-Gel process is a widely used bottom-up approach for producing nanoparticles. In this method, a sol is prepared by dissolving a precursor in a liquid, usually water, to form a stable colloidal suspension. The sol is then transformed into a gel by crosslinking, and the resulting gel is heated or calcined to form nanoparticles.

2.3.2 Hydrothermal Synthesis

Hydrothermal synthesis is a widely used technique for synthesizing nanomaterials, which involves high-pressure and high-temperature conditions in an aqueous solution. The process involves the reaction of precursors in the solution, which forms nanomaterials through nucleation and growth. The technique is versatile, allowing for control over the resulting nanomaterials' size, shape, and composition, and is commonly used in materials science and nanotechnology.

2.3.3 Co-precipitation Method

The co-precipitation method is a popular technique for synthesizing nanoparticles. It involves the simultaneous precipitation of two or more soluble salts from a solution, forming nanoparticles. This method is simple, cost-effective, and can produce highly uniform nanoparticles with a narrow distribution. The size and morphology of the nanoparticles can be precisely tuned by controlling the reaction parameters such as temperature, pH, and concentration of the starting materials. The resulting nanoparticles have many potential applications in energy storage, medicine, and electronics. In this project co-precipitation has been used for preparation if Bi_2O_3 nanostructures.

2.4 Apparatus Used

The following apparatuses are used to synthesize Bi_2O_3, RGO, and $(Bi_2O_3)_{1-x}/(RGO)_x$ (0.25, 0.50, 0.75) NCs.

2.4.1 Digital Balance

The digital balance that we have in LNT lab for the research work is USA-made, has a least count (L.C) of ± 0.001g, and has a maximum measuring limit of 320 grams. This machine is used to measure precursors for the experiment in a balanced state.

2.4.2 Magnetic Stirrer

A magnetic stirrer is a laboratory device which is used to stir or mix liquids and to bring homogeneity to the solution. It typically consists of a flat or cylindrical plate containing a rotating magnet, which creates a magnetic field. A small magnetic stir bar, placed in the liquid, is rotated by the magnetic field, stirring the liquid. Magnetic stirrers are commonly used in chemistry, biology, and medical laboratories.

2.4.3 Sonicator

At normal room temperature sonicator machine with a moderate vibrational state is used to disperse the sample in liquid for various applications.

2.4.4 Centrifuge Machine

This machine is designed to purify prepared solutions for additional processing, typically removing nitrides, chlorides, and sulfides from the solution. It has a maximum speed of 4000 revolutions per minute.

2.4.5 Electric Oven

An electric Oven evaporated the water molecules in the solutions before annealing at high temperatures. This machine has a maximum temperature range of 300C^{o}, which could be used for moisture evaporating cause without altering the sample phase and morphology.

2.4.6 Mortar and Pestle

Mortar and pestle are tools composed of hard materials c and is commonly used to grind substances into a fine powder and blend ingredients when producing nanoparticles.

2.4.7 Ceramic Crucible/Boat

The ceramic Crucible/Boat used is made of porcelain having a very high melting point (1400^{o} C) and are used to load samples for heat treatments in a furnace.

2.4.8 Furnace

In this experimental work, a furnace is used for heat treatment to get the sample's crystallinity and desired phase and morphology. This machine can operate at a maximum temperature of 1400C^{o}.

2.5 Synthesis of Bi_2O_3 Nanostructures

2.5.1 Materials

The materials which are used in this experiment are;

- For making all solutions, only De-ionized water is used.
- Bismuth (III)nitrate-pentahydrate $Bi(NO_3)_3.5H_2O$ is used as a precursor.
- Sodium hydroxide (NaOH) is used to maintain the solution's pH and as a precipitating agent.
- Ethanol and de-ionized water are used for washing.

2.5.2 Experimental Procedure

Facile synthesis of Bi_2O_3 nanoparticles has been done via the co-precipitation method. In this synthesis technique, Bismuth Nitrate Pentahydrate "$Bi(NO_3)_3.5H_2O$" is used as a

precursor, and Sodium Hydroxide (NaOH) is used as a precipitating agent.

To synthesize Bi_2O_3 nanostructures, 0.1 molar Bismuth (III)nitrate-pentahydrate $Bi(NO_3)_3.5H_2O$ solution is prepared in 100 mL of beaker using De-Ionized water. The prepared precursor solution is then magnetically stirred for about 45 minutes to obtain a white suspension (The pH of the solution was nearly 1), to which 10 Molar Sodium Hydroxide (NaOH) solution is added dropwise and ultrasonically treated in a sonicator for one hour and making the final pH of the solution 12. The resultant reaction mixture is then stirred for twelve hours to give yellowish precipitates. The as-prepared solution is then kept overnight, excess water was drained, and the residues were washed several times with deionized water and ethanol. The resultant product is then evaporated in an oven at 60ºC and grinded to a fine powder. The resultant yellowish powder is subjected to calcination at a temperature of 400 Cº in the furnace for two hours to remove the impurities and to get α-Bi_2O_3 NPs crystalline powder [38]. A general reaction of Bi_2O3 synthesis is given by the equation (3.1), and the adopted synthesis process flow chart is shown in figure (2.3).

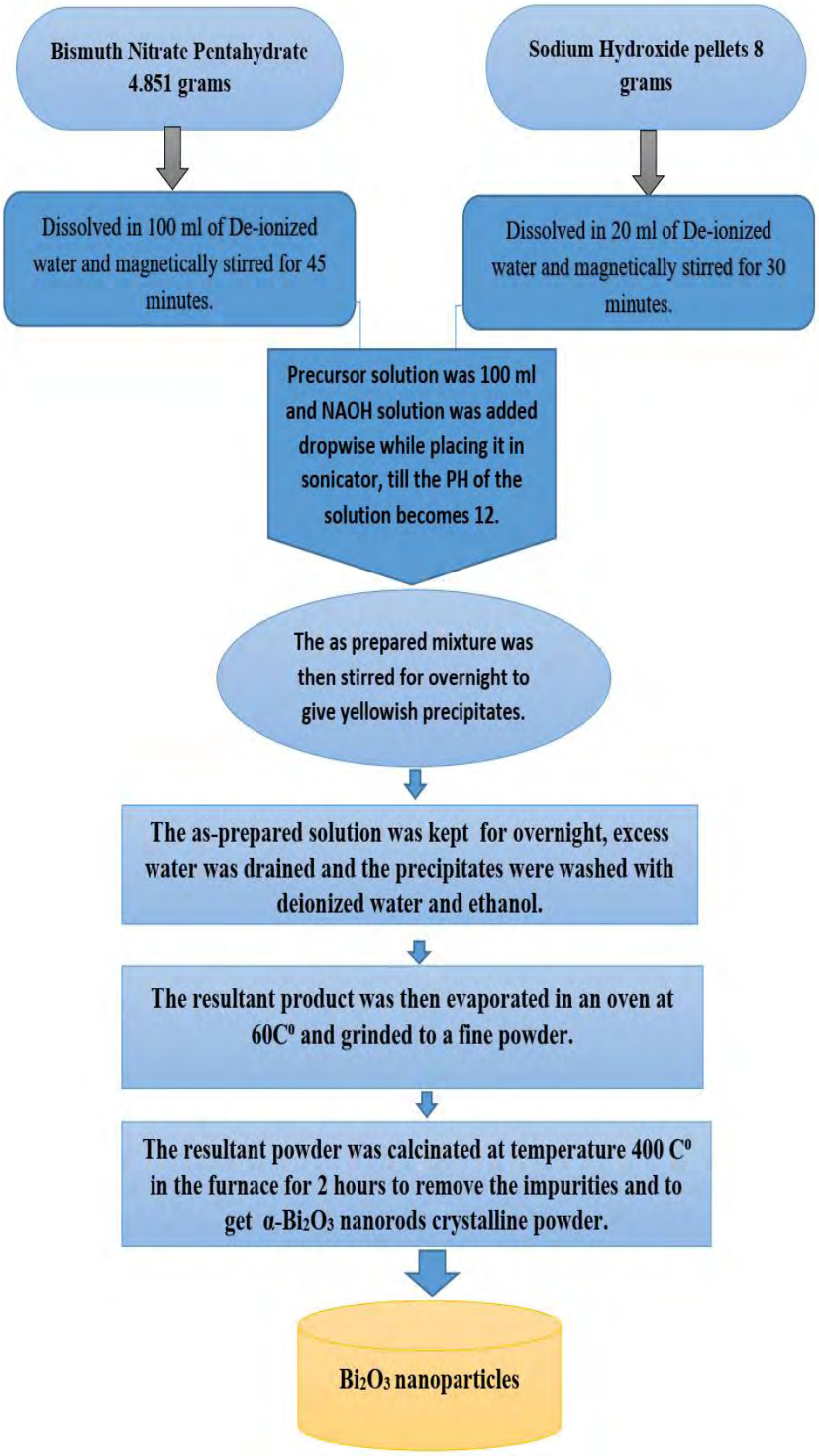

Figure 2. 3: Flow chart of Bi_2O_3 nanostructures synthesis

2.6 Synthesis of RGO

2.6.1 Materials

The materials which are used in this experiment are;

Graphite flakes (99%, sigma Aldrich), Concentrated H_2SO_4 (98 %), KMnO4 (99%, Sigma Aldrich), dilute HCl (37%), H_2O_2 (30%), hydrazine hydrate (90 %).

2.6.2 Experimental Procedure

Graphite flakes are typically used as the starting material for the synthesis of RGO. With 15 mL of concentrated sulfuric acid, 1 gram of graphite flakes were added. The solution was regularly stirred, and the suspension was prepared. Graphite flakes are oxidized by adding 6 grams of potassium permanganate ($KMnO_4$) as a strong oxidizing agent. The suspension was then agitated for 25 minutes at room temperature before being sonicated for 8 minutes in an ultrasonic bath. After agitation and sonicating the mixture, 250 mL of distilled water was added. Then, after being subjected to ultra-sonication for one hour to eliminate the graphite oxide, 30 mL of hydrogen peroxide (H_2O_2) is added and after that, 2M HCL solution (to remove excess metal ions) was added dropwise and ultrasonically treated in a sonicator for one hour, making the final pH of the solution 7. By centrifuging the mixture at 10,000 rpm, GO was repeatedly washed with distilled water. The produced GO precipitates were dried for 24 hours at room temperature.

The above suspension was once more sonicated for two hours to produce RGO. At room temperature, hydrazine hydrate was added drop by drop to the exfoliated graphite oxide suspension. The reduction was carried out for one hour at 100 C. For this sample, hydrazine hydrate and GO are maintained at a weight ratio of 9:7. The resulting black precipitates were filtered through cellulose filter paper and rinsed with distilled water and a 1M HCl solution to achieve a pH of zero. Finally, RGO is produced by drying the filtrate at room temperature for 24 hours. Figure 2.4 shows the flow chart of RGO synthesis.

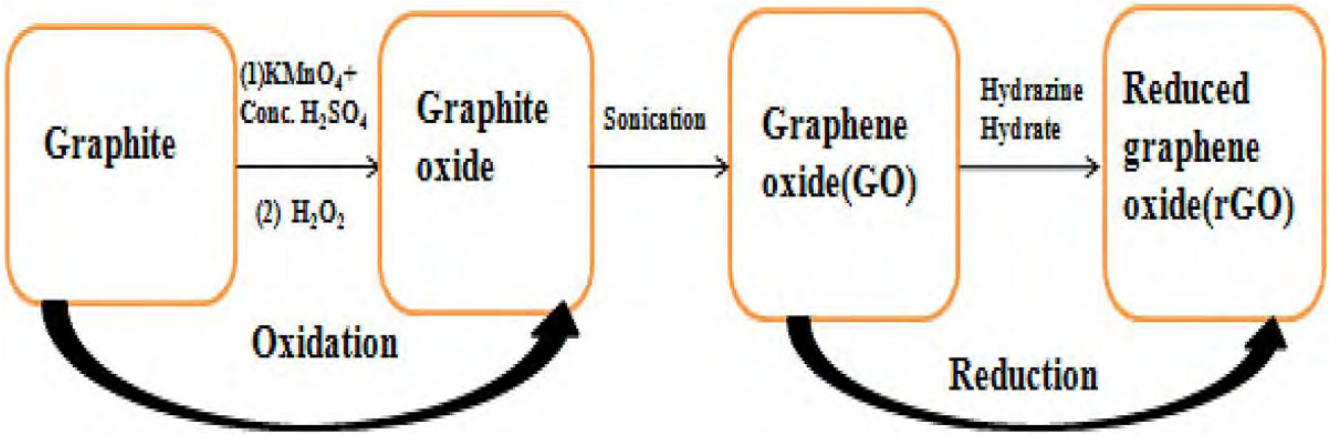

Figure 2. 4: RGO synthesis flow chart [39]

2.7 Fabrication of Bi_2O_3-RGO Nanocomposites

Generally, controlled fabrication of Bi2O3-RG0 NCs can be prepared via various synthesis routes related to two main methodologies, namely,

- In-Situ Approach
- Ex-Situ Approach

In the in-situ approach, the precursors of Bi_2O_3 are deposited on reduced graphene oxide (RGO) by a specified procedure to prepare Bi_2O_3-RGO NCs, whereas in the Ex-situ approach or often called "self-assembly" approach, host material (Bi_2O_3) and composite material (RGO) are synthesized separately via different synthesis routes and then, their appropriate ratios are bind together to get required $(Bi_2O_3)_x$ $(RGO)_{1-x}$ (where x= 1, 0.75, 0.5, 0.25 and 0) NCs. In this work, an Ex-situ approach is adopted for NC fabrication, where different ratios of both materials are bound together to get Bi_2O_3-RGO different nanocomposite ratios of the host and composite material. The adopted method is depicted in figure (2.3) to fabricate $(Bi_2O_3)_{1-x}$ $(RGO)_{1-x}$ (where x= 0, 0.25, 0.50, 0.75, 1) NCs.

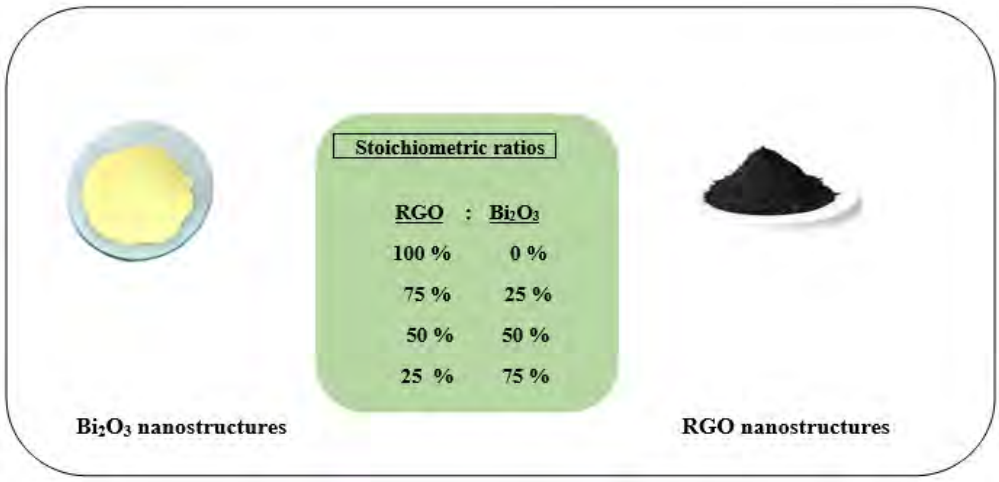

Figure 2. 5: Different ratios of Bi_2O_3 and RGO NCs fabrication

The carried-out procedure consists of three main following steps.

- Different stoichiometric ratios of the host material (Bi_2O_3) and reduced graphene oxide are transferred in an agate material mortar pestle.
- An appropriate amount of acetone is poured to make a mixture, further grounded for four hours at RT so that both materials were mixed well.
- The grounded mixture is heated in an electric oven to evaporate the remaining moisture of acetone.
- The same procedure is adopted for all the NCs.

2.8 Electrochemical Setup

2.8.1 Nickel Foam Washing and Activation

For washing the nickel foam, these steps are followed.

- For the electrochemical properties testing, nickel foam is used.
- The nickel foam should be cleaned thoroughly to remove contaminants that could interfere with the electrochemical measurements.
- Preparing nickel foam involved pretreating it with acetone and is treated ultrasonically for 30 minutes.
- Secondly, it is ultrasonically treated with 3M H_2SO_4 and is washed with ethanol, and

deionized water to eliminate any oxide layer on its surface.

- The as prepared material is then used as an active component to create a working electrode.

2.8.2 Electrode Preparation

A thick paste is made by mixing 10% activated carbon black powder, 5% polyvinylidene difluoride (PVDF), and 80% active substances in 5% N-methyl-2-pyrrolidinone (NMP), which is then spread on a Nickel foam with an area of 1cm^2. The remaining solvent is removed after heating the nickel foam at 70°C for 12 hours in an oven. The average mass of the deposited substance on the nickel foam is about 1 mg.

2.8.3 Electrolyte Preparation

The electrochemical properties of the prepared electrode are tested using 6 M KOH electrolytes. The following steps are followed to prepare the electrolyte.

- First, the required amount of KOH is calculated by multiplying the molarity (6M) by the volume (40 ml) and the molecular weight of KOH (56.11 g/mol).
  Amount of KOH (in grams) = Molarity × Volume (In Liters) × Molecular Weight
- This gives a result of 13.47 grams KOH required.
- Weigh out this amount of KOH using a weight balance and it is added into the clean and dry 100 ml beaker.
- Approximately 30 ml of distilled water is added to the beaker and then stirred the mixture with the help of a magnetic stirrer until the KOH dissolves completely.
- Finally, distilled water is added to the solution to bring the final volume to 40 ml and stir to ensure homogeneity.
- The resulting solution is 6M KOH.

Chapter No.03 Characterization Techniques

3.1 Introduction

In Material Science, characterization is a general procedure used to examine and measure the structural characteristics of various types of materials. The characterization is a key mechanism in this area of material science for learning about the scientific understanding of engineering materials [40]. Without these characterization procedures, the ascertainability of such materials is not achievable [41]. These characterization methods include "macroscopic" methods like density calculation, thermal analysis, and mechanical testing, as well as methods that look at the "microscopic" structures and properties of the material [42]. The size of material characterization varies from "Angstroms" (10^{-10} m), such as chemical bonding and individual atom imaging, up to "Centimeters" (10^{-2} m). These approaches are categorized based on their usefulness and area of expertise.

- Microscopy
- Spectroscopy
- Macroscopic Testing

3.1.1 Microscopy

This group of characterization techniques looks into and identifies the material's "Surface" and "Sub-surface" structure. "Photons, electrons, ions, or physical cantilever" are often utilized to investigate sample structure. Some of the commonly used microscopy techniques are scanning probe microscopy (SPM), Scanning Electron Microscopy (SEM), and Transmission Electron Microscopy (TEM).

3.1.2 Spectroscopy

This characterization technique category applies several principles to reveal and probe the material characteristics, including chemical composition, crystal structure, composition variation, and photoelectric properties. Some of the frequently used spectroscopy methods include Fourier Transforms Infrared Spectroscopy (FTIR), Photoluminescence (PL), X-ray Diffraction (XRD), Energy-Dispersive X-ray Spectroscopy (EDX, EDS), X-ray Photoelectron Spectroscopy (XPS), Nuclear Magnetic Resonance (NMR), and Electron Paramagnetic/Spin Resonance (EPR, ESR).

3.1.3 Macroscopic Testing

The "Macroscopic" characteristics of various materials are characterized in several ways. The most widely used techniques include Differential Thermal Analysis (DTA), Thermogravimetric Analysis (TGA), and mechanical testing (tensile, compressive, toughness, fatigue, etc).

3.2 X-Ray Diffraction (XRD)

3.2.1 Introduction

X-ray diffraction is used in Material Science to determine the crystallographic structure of the substance. When a crystallographic material is exposed to X-rays, the XRD mechanism relies on the X-ray scattering angles and intensities. One of the main applications of XRD is the manifestation of crystallographic materials based on their diffraction pattern. This technique can also be used to identify phases, which is information on how the actual structure of a crystallographic material differs from the ideal one due to internal stresses and flaws.

3.2.2 Working Principle of XRD

Bragg's Law is the fundamental working principle of XRD. It demonstrates how the incident and dispersed X-rays are related. Since crystalline materials have atomic lattice planes regularly spaced apart by “d”, they act as diffraction grating when incident rays have a wavelength corresponding to the d-spacing between the planes. XRD setup consists of the components X-ray source, sample stage, and detector. Figure 3.1 shows the basic setup of X-ray diffraction spectroscope.

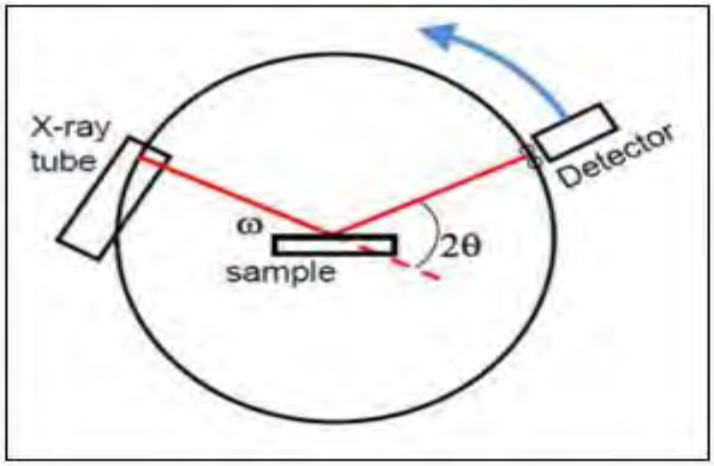

Figure 3. 1: Basic instrumentation of XRD setup [43]

As seen in Figure 3.2, a crystal with two atomic planes (1) and (2) with a fixed d spacing is an example. When rays AA' and BB' from a monochromatic electromagnetic wave collide with it, a diffraction pattern is formed.

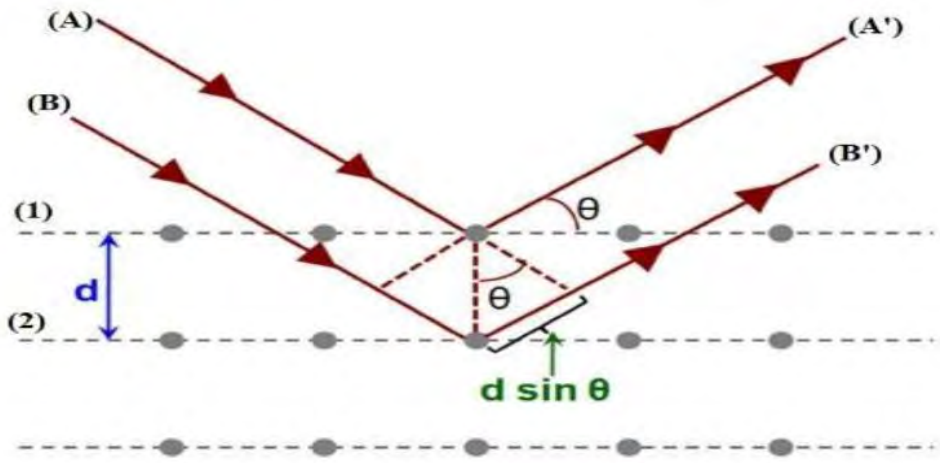

Figure 3. 2: Bragg's Law for XRD [44]

These photons can cause constructive or destructive interference depending on the path difference. Constructive interference occurs when two parallel waves of the same wavelength are in phase with one another, and destructive interference results when they are not in phase. The interference of incident waves that is both constructive and destructive is shown in Figure 3.3. For constructive interference, the path difference between the two waves should be an integral multiple of the incident wavelength, while in the case of destructive interference path difference is not an integral multiple.

$$2dSin\theta = n\lambda \qquad (3.1)$$

Equation 3.1 is the mathematical expression of Bragg's law for X-ray diffraction, where "n" is the order of diffraction, λ is the wavelength of X-ray, "d" is the interplanar spacing and "θ" is the scattering angle of an X-ray. For each set of lattice planes, X-rays diffracted at a specific angle produce a constructive interference pattern that results in the material's peak pattern called the XRD diffractogram. The information about the crystal structure is achieved by beams diffracted at different angles and with variable intensities for a particular wavelength. The

diffracted angle identifies the Bravais lattice, and the peak intensities specify the atoms that make it up. The peaks' sharpness usually shows the material's great crystallinity; peaks are sharp and vivid in crystalline materials. Samples are usually scanned at a slower scan rate 2θ from 10° to 80°. The average crystallite size of the materials can be measured using the Scherrer formula given by equation 3.2. The graphical illustration of constructive and destructive interference is depicted by the figure 3.3.

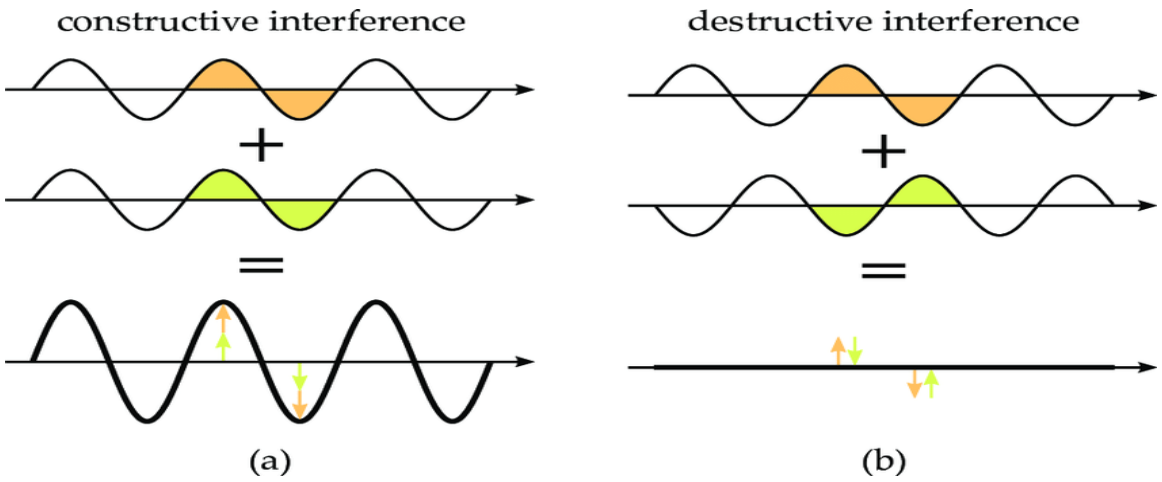

Figure 3.3: Constructive and destructive interferences [45]

The average crystallite size of the materials can be measured using the Scherrer formula given equation (3.2)

$$\mathbf{D} = \frac{\mathbf{0.9\,\lambda}}{\mathbf{w Cos\theta}} \qquad \mathbf{(3.2)}$$

Here, "λ" represents the wave's wavelength, w is the full width at half maximum (FWHM), and θ is the incident angle of the incident wave. The Crystallite size of a material is the average of all measured crystallite size values corresponding to each prominent peak in the XRD pattern. The lattice parameters for different crystal symmetries can be calculated using the link between plane spacing, lattice parameters, and miller indices.

3.3 Raman Spectroscopy

3.3.1 Introduction

Raman spectroscopy is a sophisticated scattering method that analyses samples' rotational and vibrational frequencies by utilizing both inelastic and elastic scattering of single-colour light. Raman discovered the Raman effect in 1928. Both qualitative and quantitative analyses are possible with Raman spectroscopy. Frequency of scattered light is utilized for the qualitative investigation, while intensity is used for quantitative analysis. To classify materials and establish crystal orientations, chemists typically use Raman spectroscopy. The basic instrumentation of the Raman spectroscope is illustrated by the figure 3.4.

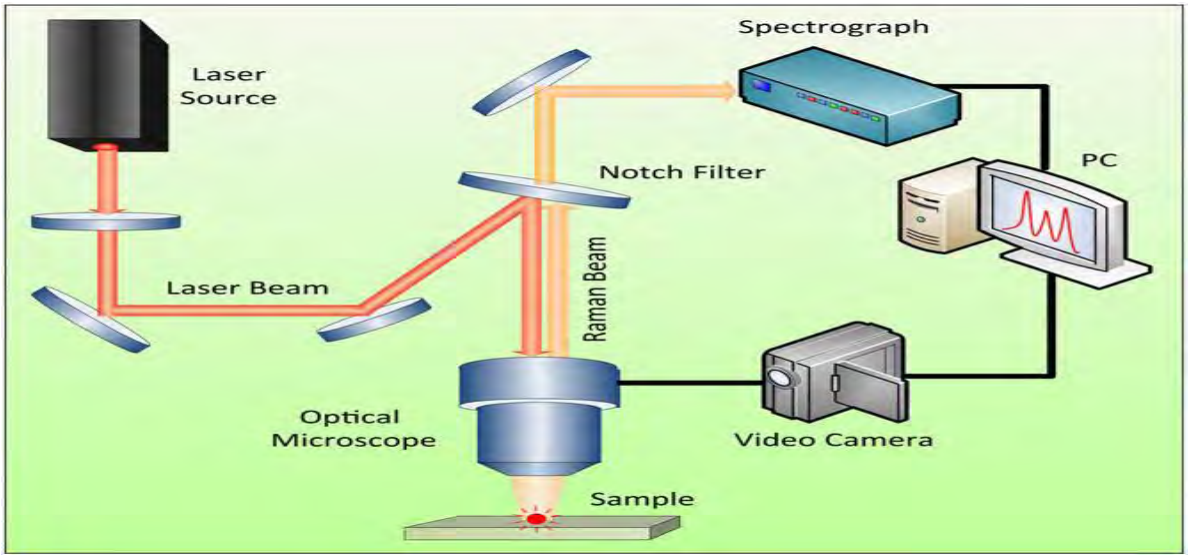

Figure 3. 4: Instrumentation of Raman spectrometer [46]

3.3.1 Working Principle of Raman Spectroscopy

A monochromatic laser beam interacts with a sample's vibrating molecules during Raman spectroscopy before scattering in all directions. Most of this scattered light is identical to frequency of the incident light because of the elastic interaction between light and sample. This scattering, known as Rayleigh scattering, is often linked to Raman non-active mode. Rayleigh scattering is explained in Classical Physics by the force that the E vector of light exerts on the electronic states of molecules. Due to this force, molecules are forced to oscillate at the same frequency as the incident light and produce radiation at the same frequency. This phenomenon is known as an electric dipole moment (E).

3.3.2 Instrumentation

The Raman spectroscopic instrument consists of the following components.

- Light source
- Objective lens
- Excitation filter
- Sample holder
- Grating
- Detector (CCD)

Laser light is an excitation source for Raman scattering and is one of the main parts of a Raman spectrometer's apparatus. Typically, SS-Lasers (Solid State lasers) are used in the latest Raman spectroscopes with different wavelength (λ) values of (532, 785, 830, 1064) nm. The resulting signals of shorter wavelengths are greater because the Raman scattering cross-section is usually higher with shorter wavelengths of the laser, and also, at shorter wavelengths, the incidence of fluorescence increases. Usually, this instrumentation uses "Fiber optics" for transmittance and collection of laser energy from the sample. Rayleigh and anti-stoke scatterings are filtered with the help of a notch/edge filter and only let the Stokes scattered light pass through the dispersion element; normally, a "Holographic" grating is used as a dispersion element. The light is detected by a CCD detector, which generates the Raman spectrum.

3.4 UV- Visible Spectroscopy

Analyzing the absorption of nanomaterials at various wavelengths is done using UV-Vis spectroscopy. The absorption spectra of a compound in solution or as a solid are obtained using ultraviolet-visible (UV–Vis) spectroscopy. Spectroscopic observations have been made of the absorbance of light or electromagnetic radiation that excites the electrons from a substance or material's first initial state (ground state) to its first excited state. The working setup of UV-vis is shown in figure (3.5).

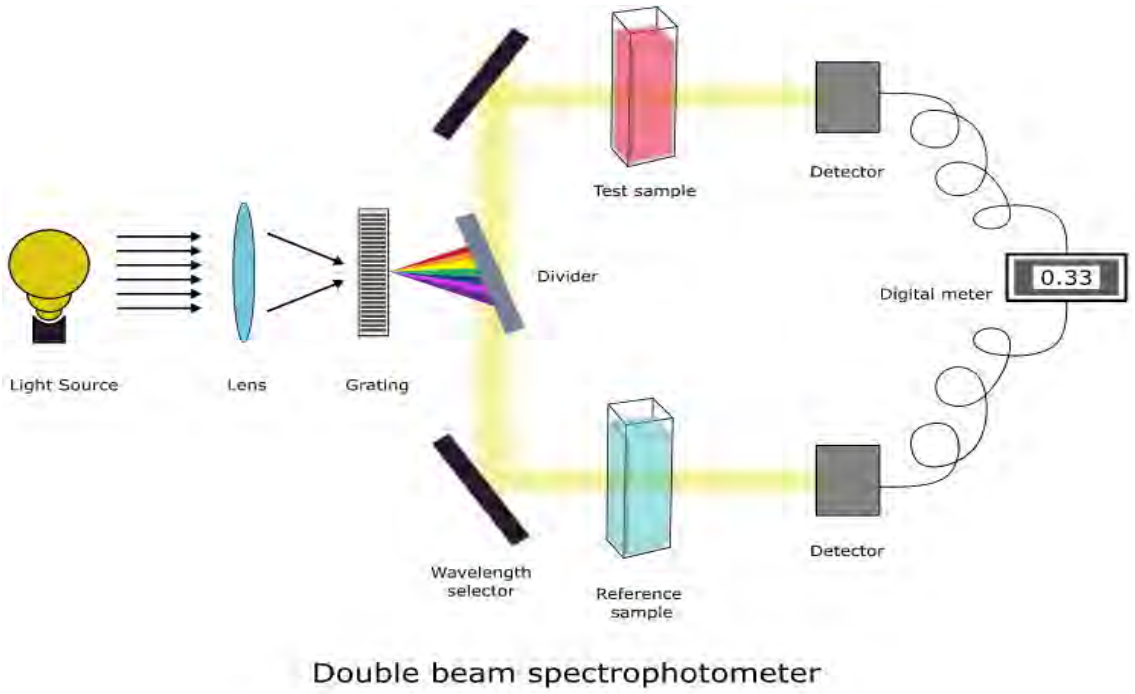

Figure 3. 5: UV-Vis dual beam spectrometer [47]

Molecules having electrons or non-bonding electrons are excited to higher anti-bonding molecular orbitals when energy from visible or ultraviolet light is absorbed. The UV-Vis spectra of organic materials are often complex and have prominent spectral bands. UV-Vis spectra of nanocomposite thin films with metal nanoclusters show surface plasmon resonance (SPR). When the inherent frequency of the electrons on the surface of nanoparticles or nanomaterial vibrating against the restoring force of positive nuclei becomes equal to the frequency of light photons, a resonance state is produced in the material.

3.4.1 Working Principle of UV-Vis Spectrometer

In Figure 3.6, a UV-Vis dual beam spectrometer's construction and functioning are depicted. A light source, monochromator, chopper, sample, and detector are among the UV-Vis system's components. The monochromator filters the radiation of the source. Then, using a chopper, pulses of the light source are directed across the sample and referenced alternately. Following the direction of both beams toward the detector, the difference between the two light intensities is calculated.

The material can be evaluated since the visible range absorption directly affects how

the materials used in UV-visible spectroscopy appear to be colored. The color is examined by the wavelength of the absorption band, λ_{max}, and absorbance at individual wavelengths. The optical absorbance (Abs) of a material is defined as the ratio of the logarithmic radiation intensity (Io) that falls on it to the radiation Intensity (I) that passes through it and is given by Equation 3.5

$$\mathbf{Abs= \log \frac{Io}{I}} \qquad \mathbf{(3.3)}$$

The increasing the beam's attenuation causes a solution's absorbance to rise. Beer's Law is an equation that connects a material's characteristics to light attenuation. According to the law, a chemical's concentration and a solution's light absorbance are related. Using a colorimeters or spectrophotometer, the relation can be used to calculate the concentration of a chemical species in a solution. Beer's Law can be expressed as;

$$\mathbf{A = \varepsilon bc} \qquad \mathbf{(3.4)}$$

Where "ε" is the molar absorptivity of the particles in solution ($M^{-1}cm^{-1}$), *b* is the path length (cm) of the cuvette, and *c* is the concentration of the solution (M). A few absorption bands that are visible in an absorption spectrum correspond to the structural groups of a particular molecule. Different substances absorb light at varied wavelengths. As a result, UV-Vis spectroscopy could be used to identify a particular sample [48].

3.5 Scanning Electron Microscopy (SEM)

The Scanning Electron Microscope (SEM) was developed in the early 1940s to study objects' structure at a microscopic level with high magnification and resolution. The electron microscope allows for direct visualization and morphological explanation of samples, making it possible to observe objects at a microscopic level. The SEM uses the wave nature of electrons to observe the sample, and different interactions occur when an electron beam interacts with the sample. These interactions include scattering, diffraction, and tunnelling through the material, which provides valuable information on the crystal structure of the sample. In summary, the SEM is an essential tool in microscopy, allowing scientists to observe and analyze samples at a microscopic level, providing invaluable insights into their morphology and structure.

3.5.1 Working Principle of SEM

The Scanning Electron Microscope (SEM) operates on the basic principle of electron scattering. The instrument emits an electron beam via thermionic emission from a tungsten filament, which is then accelerated through a high voltage, typically 21 VK, before passing through various optical systems. They scan the sample's surface, which emits electrons from its surface and is detected by different detectors in the chamber. The SEM relies on several sources, including the electron gun, condenser lenses, objective aperture, scan coils, chamber, and detectors. Two types of electron guns are used in SEM: the thermionic emission gun and the strong field emission gun. In thermionic emission, electrons are emitted by applying thermal energy to the filament, while in a field emission gun, a strong electric field is generated to emit electrons. The condenser lenses control the electron beam, allowing thin and fine adjustments to produce clear images. An objective aperture is a thin metallic sheet with four holes held by a small rod, which allows for selecting a hole of any size to pass the electron beam.

The scan coil consists of two solenoid coils, with the current in one coil changing the magnetic field in the other and vice versa. The scan coil is used to scan the sample in the specimen. It provides results using different detectors, including secondary electron emission, backscattered, X-ray, and Auger electron emission detectors [49]. When the primary electron beam strikes a sample, the secondary electron emission detector gathers the released electrons from the sample's surface. The atomic number and density of the sample are determined by the backscattered detector, which measures the intensity of the electrons that are scattered back from the sample surface.

An X-ray emission detector is used to measure the X-rays emitted when the electron beam hits the sample to ascertain its chemical composition. The sample's surface emits electrons when

it is hit by the primary electron beam, which is subsequently detected by the Auger electron emission detector. The basic instrumentation of SEM is illustrated by the figure 3.6.

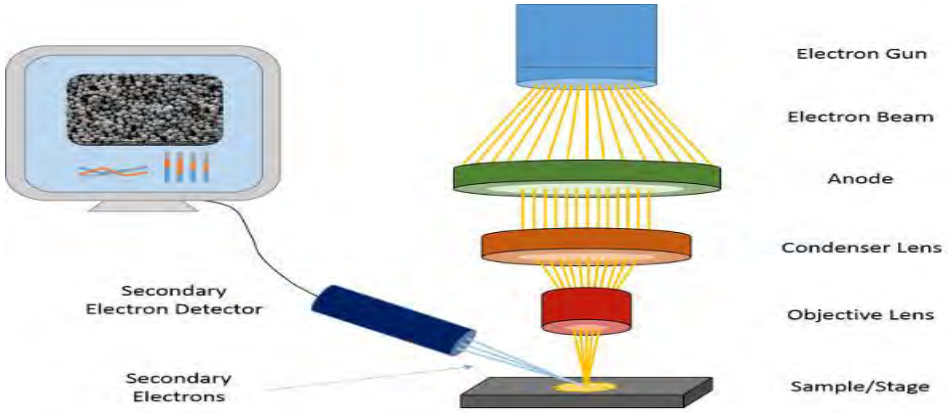

Figure 3. 6: Shows setup of scanning electron microscope (SEM) [51]

3.6 Evaluation of Supercapacitor

For energy storage devices like supercapacitors, measuring the capacity of charges, cyclic stability, energy density, and the charge-discharge rate are critical. Electrochemical Cyclic Voltammetry (CV), Galvanostatic Charge-Discharge (GCD), and Electrochemical Impedance Spectroscopy (EIS) are typically performed to calculate these parameters for supercapacitor devices. Each of these techniques provides valuable information about the performance of a supercapacitor, and they are often used together to gain a comprehensive understanding of the supercapacitor.

3.6.1 Cyclic Voltammetry

This technique measures a material's potential and current response to a cyclic change in voltage. It is used to evaluate a supercapacitor's capacitance and potential window and to identify any redox reactions that may occur during charging and discharging.

An electrode of a supercapacitor is subjected to a linearly varying electric potential during cyclic voltammetry measurements. The potential window is the term used to describe the range of the potential change, and the potential change speed is expressed in mVs^{-1}. The electrochemical reactions between the electro-active substance and the electrolyte ions are monitored through the anodic and cathodic currents. Using the cyclic voltammetry curves,

performance parameters for supercapacitors can be calculated [50]. Specific capacitance can be expressed by

$$\mathbf{Cs} = \frac{\mathbf{1}}{\boldsymbol{K\, m\Delta V}} \frac{\mathbf{1}}{\mathbf{2\pi}} \int_{\boldsymbol{Vi}}^{\boldsymbol{Vf}} \boldsymbol{I dV} \qquad \textbf{(3.5)}$$

Where "Cs" is the specific capacitance of the desired supercapacitor, "m" for the electrode's weight, ΔV is the potential window, "K" is the scan rate, and I is the current. The specific capacitance of an electrode can be determined using equation 3.5 by measuring the area of the CV curves [51].

3.6.2 Galvanostatic Charge and Discharge

The charge-discharge is an adaptable and accurate test performed with a constant current delivered to the supercapacitor device, and specific capacitance is calculated by measuring discharge time and voltage. Equation 3.8 gives the formula for the calculation of specific capacitance.

$$\mathbf{Cs} = \frac{\boldsymbol{I\Delta t}}{\boldsymbol{M\Delta V}} \qquad \textbf{(3.6)}$$

Here, Cs stands for specific capacitance, m is the mass of the material deposited on the electrode, ΔV is the potential window, and Δt is the discharge time. As illustrated in the equation, the discharge time is a significant parameter in determining the quantity of specific capacitance. It is also used to evaluate a supercapacitor's energy and power density and determine the system's rate capability.

3.6.3 Electrochemical Impedance Spectroscopy

The capacitance of devices can also be characterized via electrochemical impedance spectroscopy. This is technique that measures the impedance of a material in response to an alternating current. It is used to evaluate a supercapacitor's resistance and capacitance and identify the system's dominant resistance mechanism. When the device is supplied a modest amplitude of the alternate voltage at the open circuit potential, the signal is gathered over a large frequency range (1mHz- 1MHz). A Bode plot can be used to express capacitance. The capacitance of a device is computed using equation 3.7;

$$\mathbf{C} = \frac{\mathbf{1}}{\mathbf{2\pi fZ}} \qquad \textbf{(3.7)}$$

It is linked to the hypothetical portions of frequency "f" and impedance "Z". The capacitance is determined from the linear portion of the Bode plot, which is a log(Z) plot versus a log(f) curve. The imaginary part of impedance (Z") versus the actual part of impedance (Z') is represented by the Nyquist plots in EIS. The contact between the electrode and the electrolyte is responsible for the device's equivalent series resistance. The analogous series resistance of the device is shown on the x-axis at high frequencies. The semi-circle curve's radius represents the device's charge transfer resistance [52].

Chapter No.04 Results and Discussions

4.1 Structural Investigations

The structural properties and phase formation of Bi_2O_3 have been identified using the X-ray diffraction technique at room temperature using the Cu-k α-rays as the source, with λ $K_{\alpha 1}$ ~1.542591 Å (0.154nm), K_{α}~1.51452Å and K_{β}~1.53157 Å, having values of 35 mA accelerating current and voltage of 40 KV. The diffraction measurements of prepared Bi_2O_3 NPs have been performed in the range (15-65)º 2θ angle with step size of 0.02 in one second integration time. The XRD structure of the synthesized Bi_2O_3 NPs is in figure (4.1).

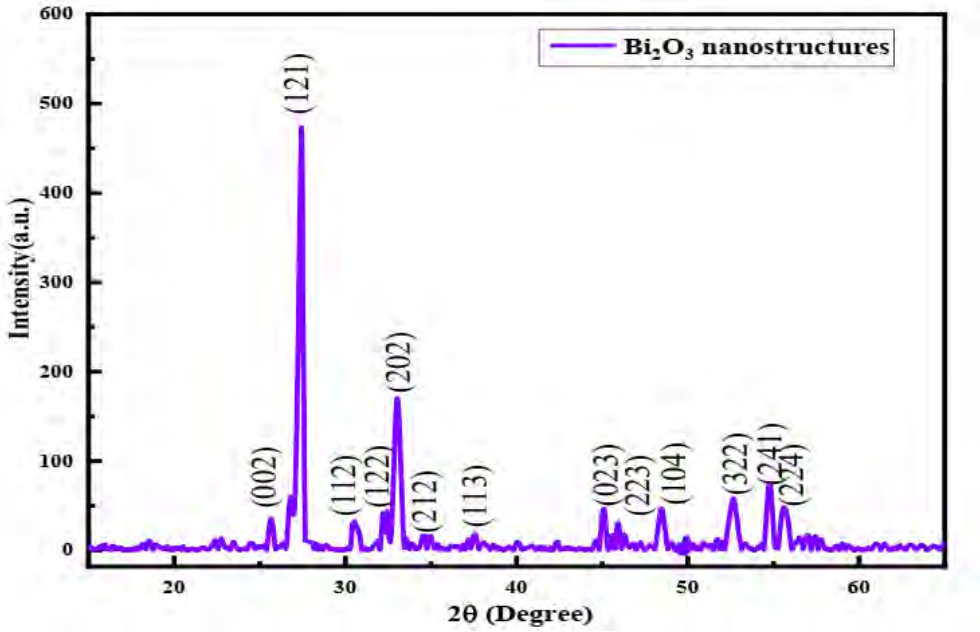

Figure 4. 1: Typical X-ray diffraction patterns of Bi_2O_3 nanostructures

The peaks with high intensity of Bi_2O_3 nanostructures originated at 2θ angles 26.906º (112), 27.387º (121), 33.229º (202), 35.037º (212), 37.572º (113), 45.139º (023), 46.289º (223), 48.594º (104), 52.378º (322), 54.798º (241) and 55.455º (224) are well indexed to standard diffraction patterns with standard (JCPD) data card number (00-027-0053). The presence of all Bi_2O_3 diffraction peaks and lack of any extra impurity peaks confirms formation of pure single phase Bi_2O_3 sample [53].

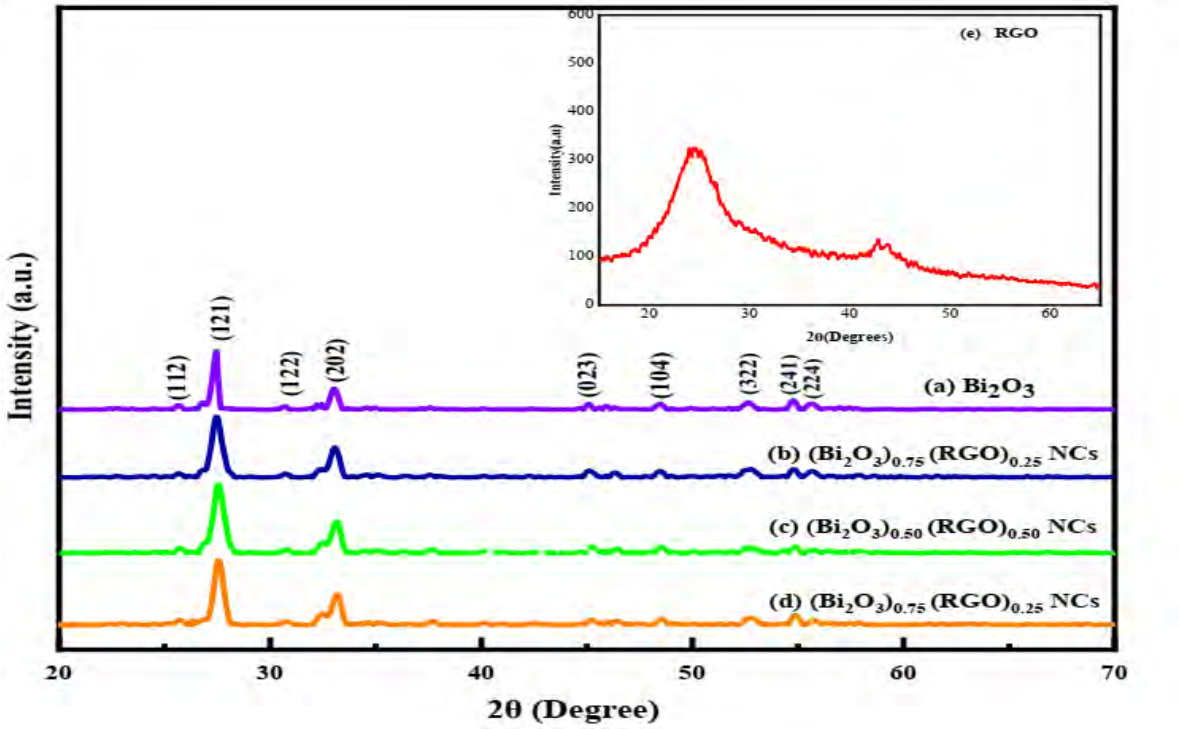

Figure 4. 2: X-ray diffraction patterns of (a) Bi_2O_3 (b) $(Bi_2O_3)_{0.75}/(RGO)_{0.25}$ NC (c) $(Bi_2O_3)_{0.50}/(RGO)_{0.50}$ NC (d) $(Bi_2O_3)_{0.25}/(RGO)_{0.75}$ NC and (e) RGO

Figure (4.2) depicts diffraction patterns of NCs and pure Bi_2O_3 and RGO. The presence of RGO peaks along with peaks of the host matrix in figures 4.3 (b, c, d) confirms the successful formation of $(Bi_2O_3)_{1-x}/(GNPs)_x$ (x= 0.25, 0.50 and 0.75) NCs. The x-ray diffraction patterns of the nanocomposites $(Bi_2O_3)_{1-x}/(RGO)_x$ (x= 0, 0.25, 0.50, 0.75, 1) materials are well indexed with literature [54]. The NCs patterns show broadening of peaks width with the increase concentration of RGO, which suggest the successful incorporation in the host matrix. Diffraction patterns of NCs depict clearly characterized peaks of RGO according to the literature, where these humps are located at the 2θ angles, 24.4778°, 42.7906° and 43.8030°. It can be observed from patterns that the peaks of Bi_2O_3 and NCs are slightly shifted towards higher 2θ angles with RGO addition which is due to apparent decrease in crystallite size, presence of strain dislocations, and agglomeration of NCs [55].

The crystallite sizes and lattice parameters have been calculated using the Deby Scherrer formula given by the equations 4.1 and 4.2.

$$\mathbf{D = \frac{0.94\lambda}{\beta\cos\theta}} \qquad \mathbf{(4.\ 1)}$$

Here, 'D' is the average crystallite size of the particle, λ corresponds to the wavelength of the Cu-Kα source, β is full width at half maximum (FWHM) and 'θ' corresponds to Brag's angle.

$$\mathbf{a = d\sqrt{h^2 + k^2 + l^2}} \qquad \mathbf{(4.\ 2)}$$

Here, 'a' is the lattice parameter constant, 'h', 'k' and 'l' represent the miller indices and 'd' corresponds to the inter-planar spacing of the parallel planes. It is observed from these spectra that, with increasing the RGO content the crystallite sizes of NCs decreases. The appearing decrement in the crystallite sizes and increase in strain dislocations in NC_s with increase concentration of RGO can be attributed to the present plenty of oxygen defects on the surface of Bi_2O_3 [56]. The estimated crystallite sizes and corresponding lattice parameters and strain dislocations are tabulated in table (4.1).

Table 4.1: Average crystallite sizes and lattice parameters of Bi_2O_3, RGO, and $(Bi_2O_3)_{0.50}/(RGO)_{0.50}$ NC

Material	Lattice Parameter (A°)	Crystallite size (nm)
Bi_2O_3	a=5.9, b=8.2, c=7.5	55
$(Bi_2O_3)_{0.50}(RGO)_{0.50}$	a=3.9, =3.9, c=13.7	25
RGO	a=5.6, b=5.6, c=5.6	15

4.2 Vibrational Analysis

The FTIR spectra of pristine Bi_2O_3, RGO and their nanocomposite $(Bi_2O_3)_{0.50}/(RGO)_{0.50}$ are recorded in the range (400–4000) cm^{-1} using a KBr pellet as a reference for Fourier transformation. The chemical bonding in the Bi_2O_3, RGO and $(Bi_2O_3)_{0.50}/(RGO)_{0.50}$ nanocomposite can be clearly observed in figure (4.3). In the spectrum of pure Bi_2O_3, the bands are observed at 1382 cm^{-1},668 cm^{-1}, and 589 cm^{-1} which are attributed to the Bi-O stretching vibrations. The strong absorption bands at 1293 cm^{-1} and 845 cm^{-1} are assigned to the Bi-O-Bi stretching vibrations. The band around 1042 cm^{-1} corresponds to the O-O stretching vibrations. FTIR spectra of the pure RGO show major absorption bands at 2351 cm^{-1}, 1701 cm^{-1}, and 1568 cm^{-1} for the stretching

vibrations O-H, C=O and C=C, respectively. The main characteristic bands of Bi-O-Bi and Bi-O stretching vibration in pure Bi_2O_3 show a slight shift toward lower wave number in $(Bi_2O_3)_{0.50}/(RGO)_{0.50}$ composite. This shift clearly confirms the formation of close interaction between the Bi_2O_3 and RGO counterparts in the final product of composite.

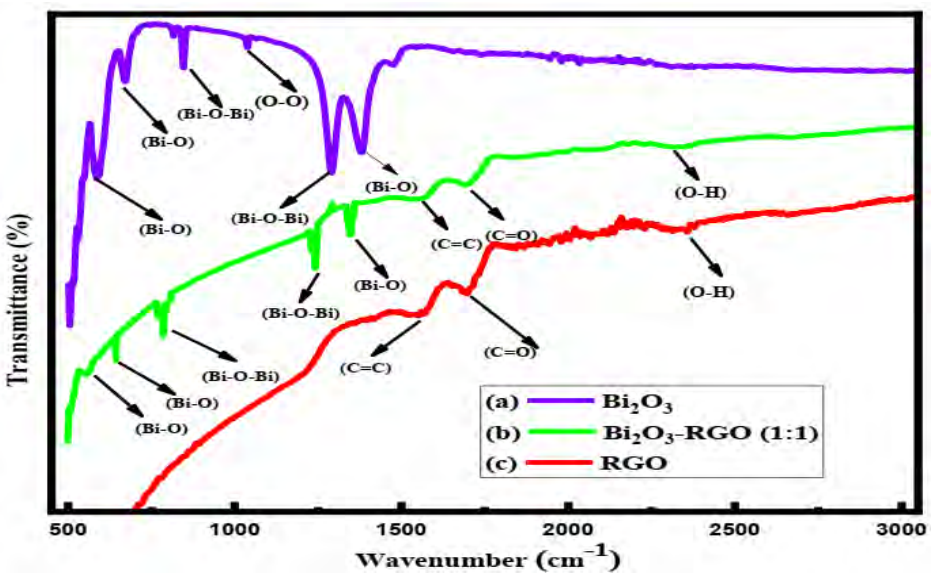

Figure 4. 3: FTIR spectra of (a) Bi_2O_3, (b) $(Bi_2O_3)_{0.50}/(RGO)_{0.50}$ NC, and (c) RGO

4.3 Optical Studies

The optical properties of synthesized Bi_2O_3, RGO nanostructures and $(Bi_2O_3)_{1-x}/(RGO)x$ (x= 0.25, 0.50 and 0.75) NCs have been studied using UV-visible spectroscopy in a wavelength range of (200-800) nm at normal room temperature ~27 C°. The values of energy band gap of synthesized nanocomposites have been calculated using well-known Tauc's relation using equations 4.3 and 4.4.

$$\alpha = \frac{2.303(A)}{t} \qquad (4.3)$$

$$(\alpha h\nu)^2 = A\,(h\nu - E_g) \qquad (4.4)$$

Where,

'α' is the absorption coefficient,

'A' refers to absorbance and correspondso bandgap energy,

't' cuvette thickness,

'hν' represents photon energy,

The exponent two shows the nature of transition, which corresponds to the direct band gap of the materials. The energy band gap of a material can be determined using Tauc's relation and it is useful in understanding electronic properties. Optical absorption spectroscopy is used to test how the different materials absorbs light at various photon energies (hν). The energy band gap (E_g) is the point in the plot where tangent to the curve at the point of intersection meets the x-axis when $(\alpha h\nu)^2$ is plotted against photon energy (hν).

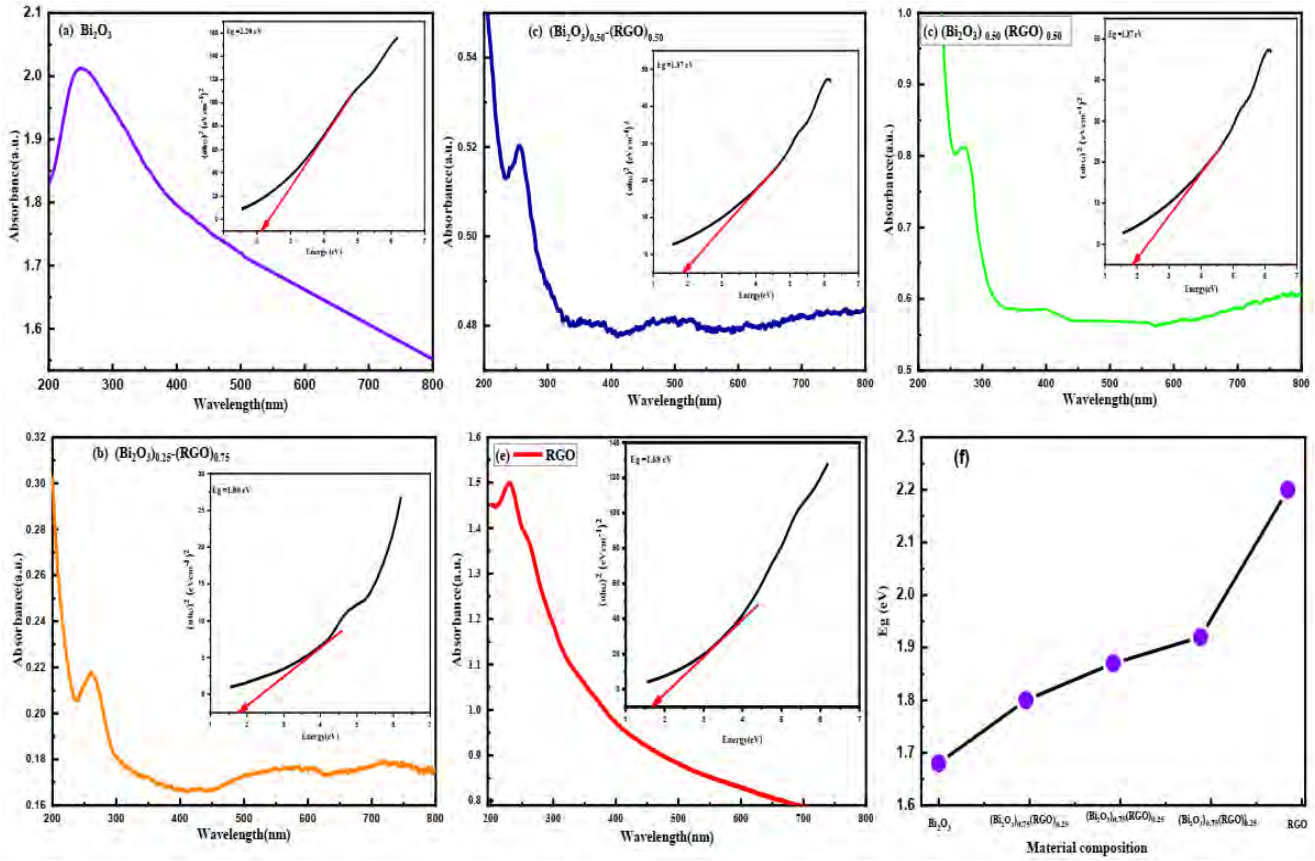

Figure 4.4: UV-Visible absorption spectra of (a) Bi_2O_3, (b) $(Bi_2O_3)_{0.75}/(RGO)_{0.25}$ NC, (c) $(Bi_2O_3)_{0.50}/(RGO)_{0.50}$ NC, (d) $(Bi_2O_3)_{0.25}/(RGO)_{0.75}$ NC (e) RGO and (f) Ragone plot of E_g vs material composition

In Fig. 4.4, it can be seen that (a) Bi_2O_3, (b) $(Bi_2O_3)_{0.75}/(RGO)_{0.25}$ NCs, (c) $(Bi_2O_3)_{0.50}/(RGO)_{0.50}$ NCs, (d) $(Bi_2O_3)_{0.25}/(RGO)_{0.75}$ NCs and (e) RGO have clear absorption peaks at around 251 nm, 255 nm, 270 nm, 260 nm and 229 nm respectively in the visible-light regions. In the above graphs, the inset shows the $(\alpha h\nu)^2$ plot as a function of photon energy ($h\boldsymbol{\nu}$). Compared with the UV-visible spectra of the pure Bi_2O_3 and RGO nanomaterials, the absorption edge of the $(Bi_2O_3)_{0.75}/(RGO)_{0.25}$ NCs, $(Bi_2O_3)_{0.50}/(RGO)_{0.50}$ NCs, $(Bi_2O_3)_{0.25}/(RGO)_{0.75}$ NCs exhibit a slight shift into the higher wavelengths, 255 nm, 270 nm, and 260 nm, respectively. The creation of a single phase is confirmed by the existence of a single peak in all spectra, which also validates the findings of XRD and FTIR about the phase purity of the samples. The band gap energy values for the pure Bi_2O_3, RGO, and their nanocomposites $(Bi_2O_3)_{1-x}/(RGO)_x$ for x = 0.25, 0.50 and 0.75 have been determined and are found to be 2.20, 1.68 eV, 1.92, 1.87 and 1.80 respectively. The Ragone plot between the E_g verse sample code is shown in figure 4.4 (f).

Figure 4. 5: Variation in band gap energy with varying concentration of RGO in host material Bi_2O_3

As the concentration of RGO in the host material Bi_2O_3. nanomaterial increases, the band gap value decreases. Charge transfer between RGO and Bi_2O_3 can be facilitated by RGO acting as an electron acceptor. The electrical structure of both materials and their respective band gaps reduces because of this charge transfer and quantum confinement processes. The interactions between the two components are optimal in $(Bi_2O_3)_{0.50}/(RGO)_{0.50}$ NCs as the ratio of Bi_2O_3 to RGO

is balanced so due to efficient charge transfer and quantum confinement processes, this balanced composition can lead to the greatest reduction in band gap energy. The materials' electronic conductivity is improved by this minimum energy band gap for the composite material, which is used as an electrode, and thus, it results in high specific capacitance (Cs).

The optical band gap energies have been calculated by drawing a tangent to the root of absorbance, time energy along the y-axis $(\alpha h\nu)_2$ and energy along the x-axis ($h\nu$) as illustrated in figure (4.3).

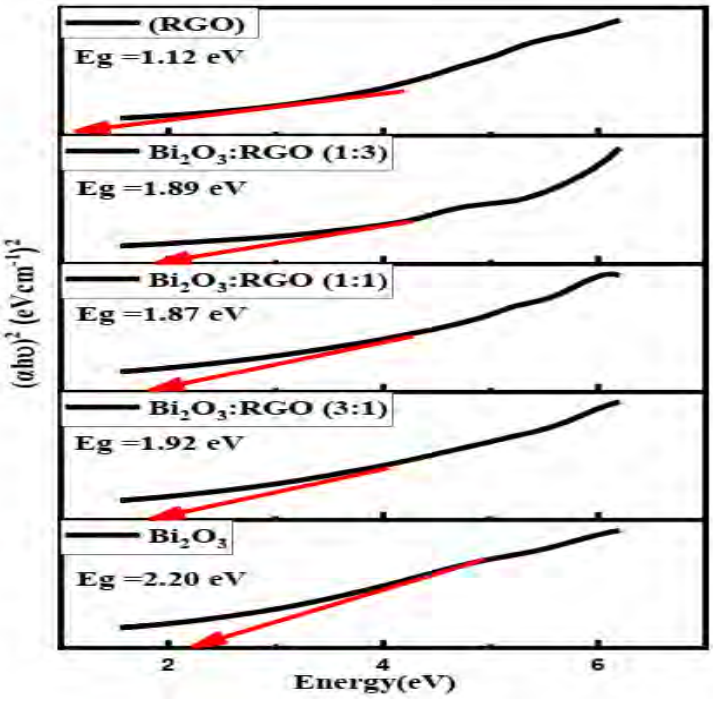

Figure 4. 6: Variation in band gap energy with varying concentration of RGO in host material Bi_2O_3

The results demonstrate that intermediate Nano-compositions optical band gaps have been controlled, demonstrating their semiconductor character. This visible light bandgap nanomaterial can be used for photocatalysis, LEDs and supercapacitor applications**.**

4.4 Electrochemical Properties

4.4.1 Cyclic Voltammetry (CV)

As a supercapacitor electrode material, the prepared $(Bi_2O_3)_{1-x}/(RGO)_x$ nanocomposites have been subjected to standard Cyclic Voltammetry measurement (CV). In the standard CV system, Ag-AgCl is the reference electrode, Platinum wire is the counter electrode, and Nickel foam is the working electrode. Six molar solution of KOH is utilized as a meduium in the CV measurement

of the prepared electrode of nanocomposites. The CV curves have been scanned between 5-100 mV/s for a potential window with a fixed value of 0 V to 0.6 V.

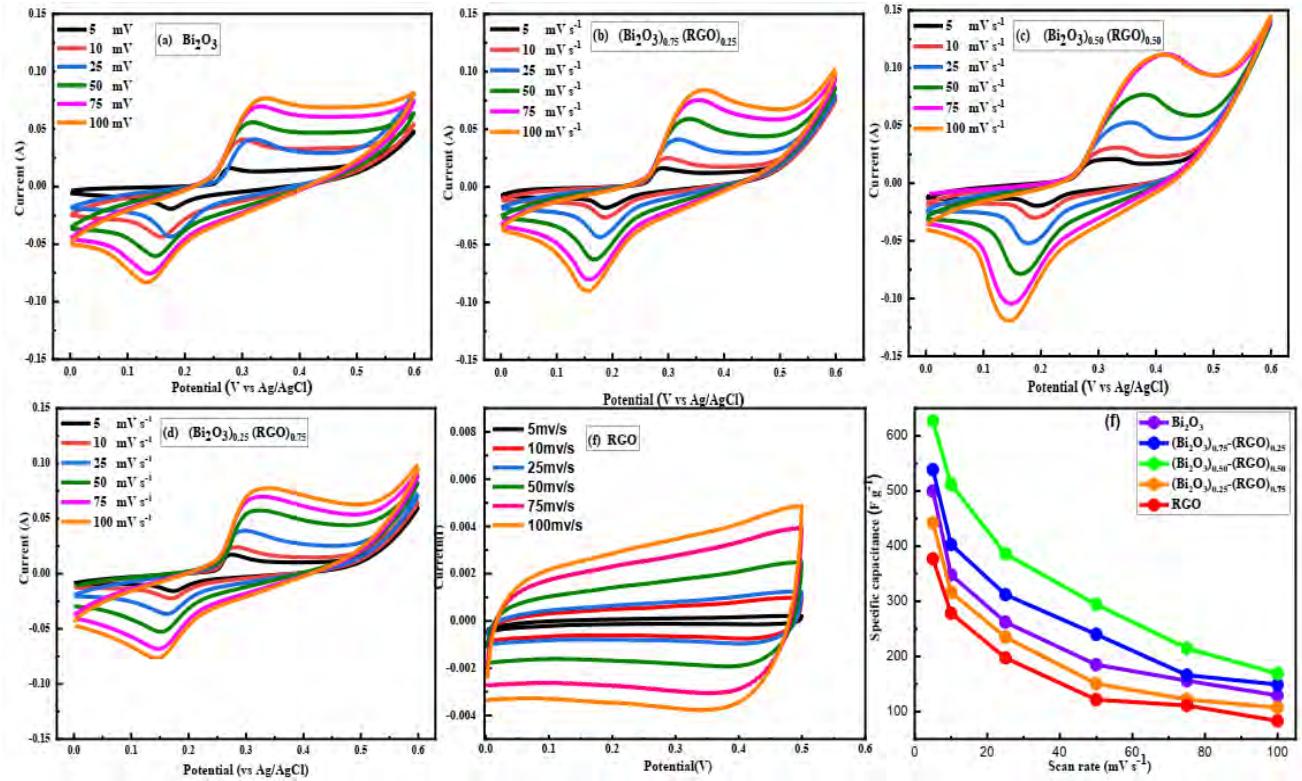

Figure 4. 7: CV curves between 5-100 mV/s scan rate of (a) Bi_2O_3 (b) $(Bi_2O_3)_{0.75}/(RGO)_{0.25}$ NC (c) $(Bi_2O_3)_{0.50}/(RGO)_{0.50}$ NC (d) $(Bi_2O_3)_{0.25}/(RGO)_{0.75}$ (e) RGO and (f) ragone plot of C_s vs Scan rate

The specific capacitance of the synthesized composite material has been calculated using equation 4.5,

$$C_s = \frac{A}{kmV} \qquad (4.5)$$

In this case, "A" represents the CV curve's area, "m" stands for the mass of active materials, "k" for the scan rate, and "ΔV" for the chosen potential window. The CV curves' shape and redox peaks indicate that the nanocomposites behave like pseudocapacitors. The specific capacitance trend falls from 5 to 100 mV/s as the scan rate increases. The ions' inability to have enough time to reach the inner layer of the active materials explains this. It is observed that the scanning rate increases, the oxidation peak moves towards the positive electrode, and the reduction peak moves towards the negative electrode, indicating that the electrode material has some internal resistance.

In comparison to the capacitance of the individual constituents, Bi_2O_3 (1000 F/g) and RGO (753 F/g), the computed specific capacitance of nanocomposites $(Bi_2O_3)_{0.50}/(RGO)_{0.50}$ is increased up to 1254 F/g. This increase in specific capacitance could result from RGO's conducting nature and Bi_2O_3 redox behaviour[57]. Bi_2O_3 at varying concentrations in RGO involves additional states around the Fermi level, which improves electrochemical performance and aids in charge storage. The Strong synergistic connections between pure Bi_2O_3 and RGO surfaces are created by the composition of $(Bi_2O_3)_{1-x}/(RGO)_x$, which enhanced the sample's electrochemical performance. The high surface-to-volume ratio and small crystallite size of composites improve their pseudocapacitive performance by allowing more ions to pass through the electrode surface. At a lower scan rate, electrolyte and electrode are in contact for a long. As a result, more charge is stored on the electrode surface, with high capacitance. The specific capacitance of Bi_2O_3, RGO, and their nanocomposites in 6M KOH electrolyte is measured at different scan rates (5-100 mV/s).

Table 4. 2: Specific Capacitance (C_s) values calculated from cyclic CV curves

Scan rate (mV/s)	**Specific Capacitance(F/g)**				
	Bi_2O_3	**Bi_2O_3/RGO(3:1)**	**Bi_2O_3/RGO(1:1)**	**Bi_2O_3/RGO(1:3)**	**RGO**
5 mV/s	1000.072	1077.31	1254.964	884.736	753.644
10 mV/s	697.686	806.916	1024.846	632.266	556.872
25 mV/s	525.916	625.424	772.060	469.662	394.398
50 mV/s	369.914	481.382	588.120	310.370	243.094
75 mV/s	311.780	332.682	429.510	245.300	222.006
100 mV/s	258.342	298.776	337.452	215.248	166.152

Bar graphs illustrating the specific capacitance of an electrode which is taken by CV at various scan rates (k) provides more clear visual plots that how the specific capacitance of the materials varies under different scan rates (k).

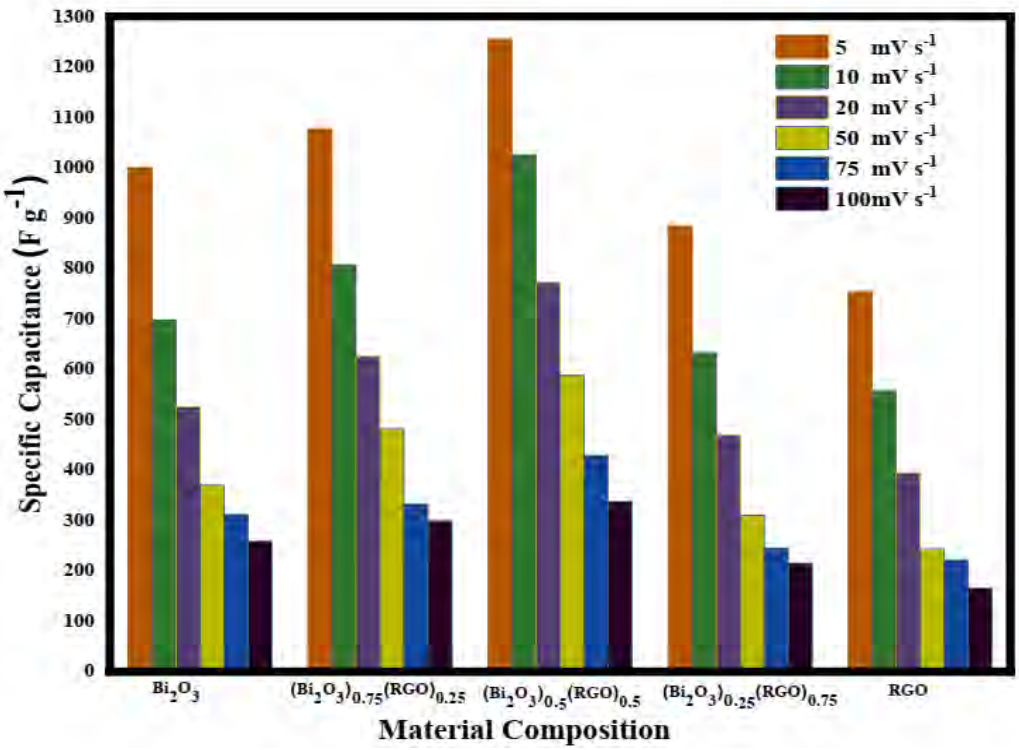

Figure 4.8: Bar graphs of CV specific capacitances (Cs) at different scan rates (5-100 mV/s) of Bi_2O_3, $(Bi_2O_3)_{0.75}/(RGO)_{0.25}$, $(Bi_2O_3)_{0.50}/(RGO)_{0.50}$, $(Bi_2O_3)_{0.25}/(RGO)_{0.75}$ and RGO respectively

4.4.2 Galvanostatic Charge-Discharge (GCD) Characteristics

The GCD measurements have been caried out to further analyze the charge storage behaviors, maintaining all samples' (0.0–0.5)V potential window. The GCD measurements of all synthesized samples have been carried out at current densities of 1, 1.5, 2 and 2.5 A/g using a three-electrode system,. The specific capacitance (C_s), energy density (E_g) and power density (P_g) of the symmetric supercapacitor have been calculated using the equations (4.6), (4.7) and (4.8) respectively.

$$C_s = \frac{I \times \Delta t}{\Delta V \times m} \qquad (4.6)$$

$$E_g = \frac{1}{2} Cs\, \Delta V^2 \qquad (4.7)$$

$$P_g = \frac{Eg}{\Delta t} \qquad (4.8)$$

In this case, "Δt" denotes the discharge duration (s), "ΔV" is the potential range, and I/m stands for current density in the units of (A/g). Bi_2O_3 and RGO nanoparticles have specific

capacitances of 646 and 476 F/g respectively at a current density of 1 A/g while $(Bi_2O_3)_{0.5}/(RGO)_{0.50}$ NCs has Cs value of 804 F/g, higher than a pure sample. The $(Bi_2O_3)_x/(RGO)_{1-x}$ (x= 0.75, 0.5, 0.25) NCs demonstrate a pseudocapacitive behavior which is due to the faradic nature of Bi_2O_3 and the results are consistent with the earlier CV findings.

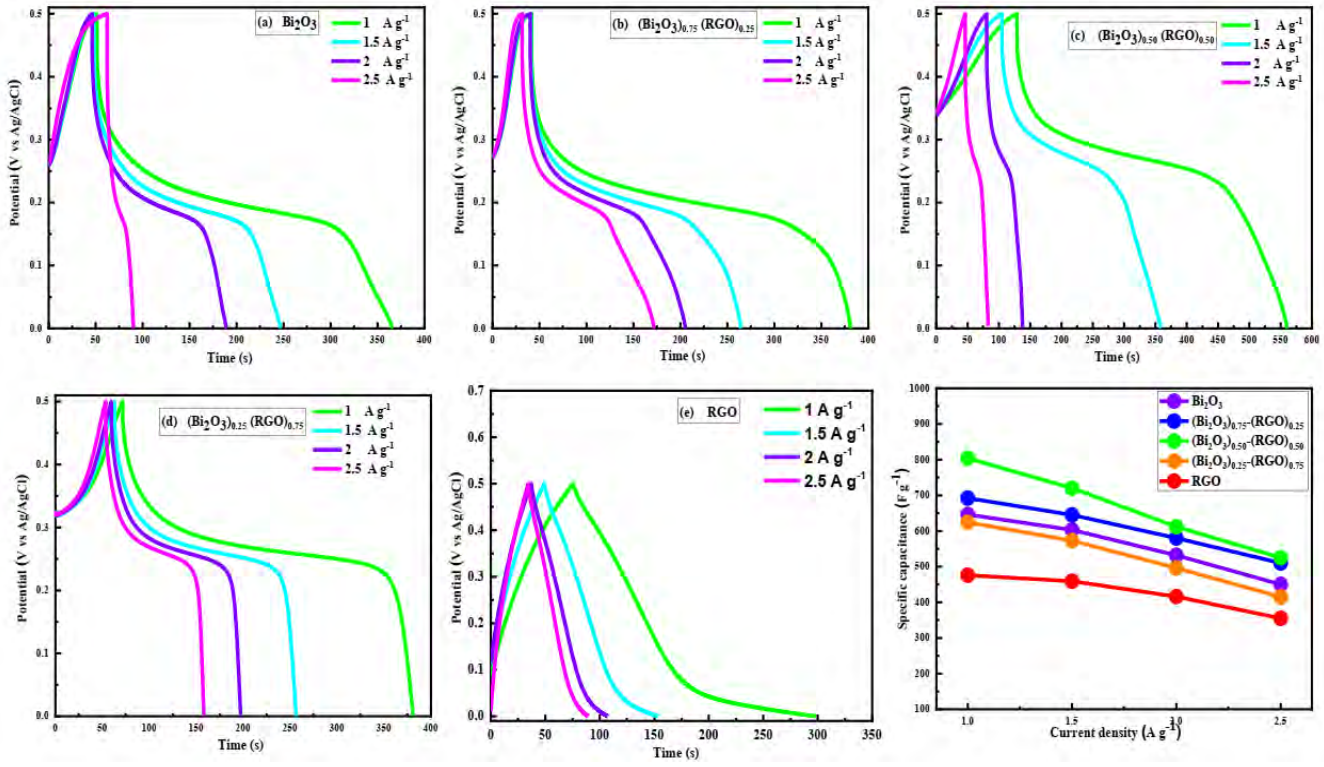

Figure 4.9: GCD plots of (a) Bi_2O_3, (b) $(Bi_2O_3)_{0.75}/(RGO)_{0.25}$, (c) $(Bi_2O_3)_{0.50}/(RGO)_{0.50}$, (d) $(Bi_2O_3)_{0.25}/(RGO)_{0.75}$, (e) RGO and (f) Ragone plot of C_s vs current density

All samples' specific capacitances have been determined using GCD graphs at different current densities of (1 A/g to 2.5 A/g). The results indicate that the $(Bi_2O_3)_{0.50}/(RGO)_{0.50}$ nanocomposite has the highest specific capacitance of 804 F/g which is greater than the pure Bi_2O_3 and RGO having specific capacitances of 676 F/g and 444 F/g respectively, obtained from GCD. The energy density and power density that have been calculated for $(Bi_2O_3)_{0.50}/(RGO)_{0.50}$ is 27 Wh/kg and 900 W/kg, respectively. The figure (4.8) also shows that the diffusion control mechanism in the electrochemical capacitor causes the Cs values to decrease as the current density rises. This is because the material's low specific capacitance Cs, which inhibits ion migration to the material's inner and active layers, provides a rapid charging rate at high current densities [58].

The specific capacitance of Bi_2O_3, RGO, and their nanocomposites in 6 M KOH is given at different Current densities(1, 1.5, 2 & 2.5)A/g.

Table 4.3: Specific capacitance values that have been obtained from GCD curves of Bi_2O_3, RGO and $(Bi_2O_3)_x/(RGO)_{1-x}$ (x= 0.75, 0.5, 0.25) NCs

Current density (A/g)	**Specific Capacitance(F/g)**				
	Bi_2O_3	**Bi_2O_3/RGO(3:1)**	**Bi_2O_3/RGO(1:1)**	**Bi_2O_3/RGO(1:3)**	**RGO**
1 A/g	646	692	804	624	476
1.5 A/g	603	645	720	573	459
2 A/g	532	580	612	496	416
2.5 A/g	450	510	525	415	355

In the table specific capacitance of an electrode which is taken by GCD at various current densities can also be clearly expressed through bar graphs. These graphs provide a clear visual picture that how the specific capacitance of the electrode material varies under different electrical current densities.

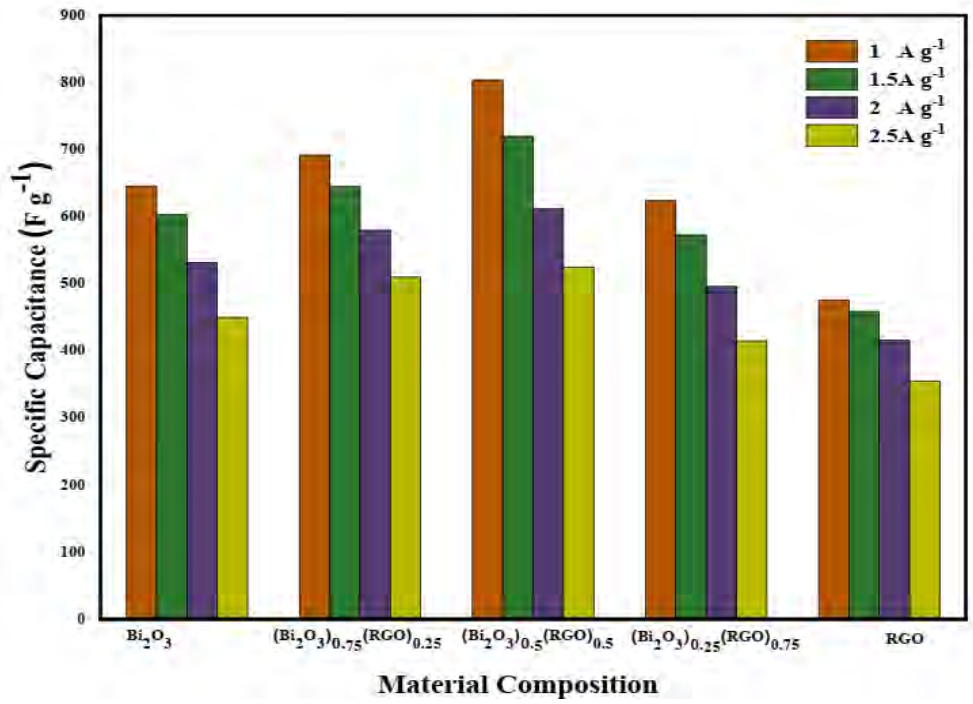

Figure 4. 10: Bar graphs of GCD specific capacitance at different current densities of Bi_2O_3, $(Bi_2O_3)_{0.75}(RGO)_{0.25}$, $(Bi_2O_3)_{0.50}(RGO)_{0.50}$, $(Bi_2O_3)_{0.25}(RGO)_{0.75}$ and RGO

4.4.3 Electrochemical Impedance Spectroscopy (EIS)

Electrochemical Impedance Spectroscopy (EIS) has been conducted using three-electrodes configuration system in a 6M KOH electrolyte with a 0.1 Hz to 100,000 Hz frequency range. The values of ESR are found to be 0.562 Ω, 0.558 Ω, 0.541 Ω, 0.548 Ω, and 0.672 Ω for $(Bi_2O_3)_{1-x}/(RGO)_x$ (x= 0, 0.25, 0.50, 0.75, 1) respectively. The lowest ESR value of 0.541 Ω is observed for 50% RGO substituted NCs, indicating an enhancement in electronic conductivity and a slight reduction in cell resistance. These results are consistent with the CV and GCD observations. The Nyquist plots has been showed a semi-circle indicative of a pseudocapacitance, a 45º short line representing a Warburg element in the equivalent circuit and a nearly ≈90º line indicating capacitive behavior. As the concentration of RGO in the samples is increased, there is a tendency towards a 45º angle, and the 50% RGO substituted NCs has been showed the highest capacitive behavior, making it a promising pseudocapacitance electrode material.

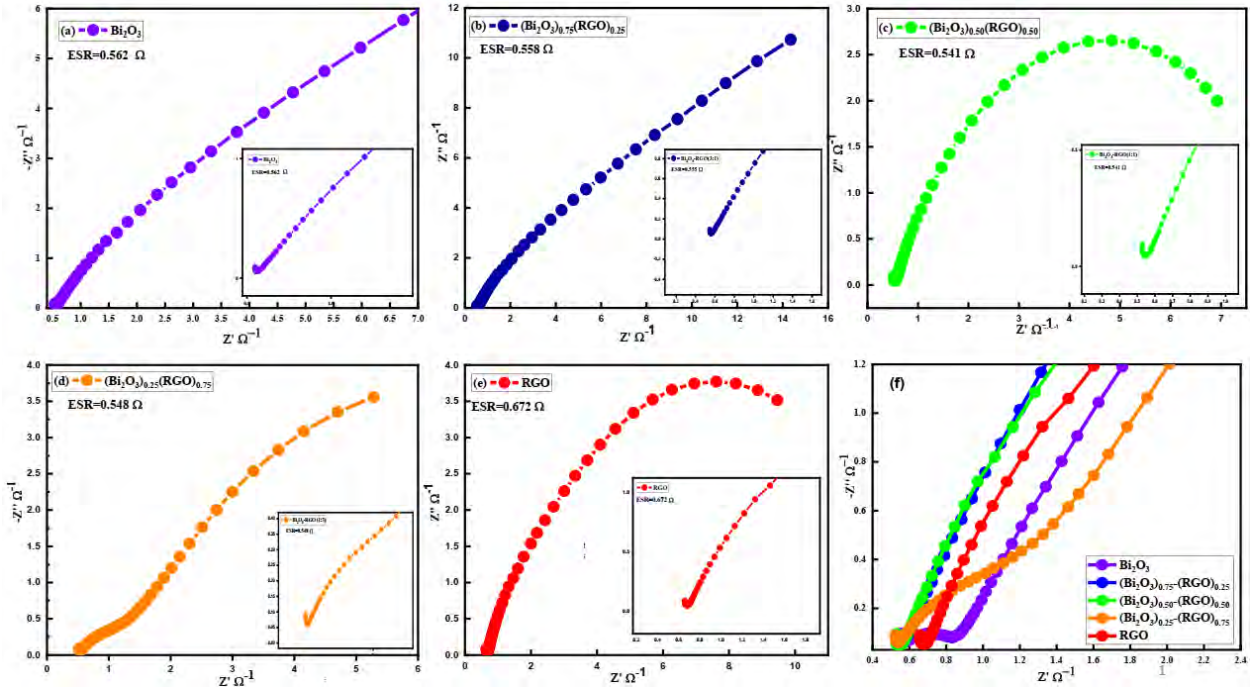

Figure 4.11: EIS Nyquist plots of a) Bi_2O_3, b) $(Bi_2O_3)_{0.75}/(RGO)_{0.25}$ c) $(Bi_2O_3)_{0.50}/(RGO)_{0.50}$ d) $(Bi_2O_3)_{0.25}/(RGO)_{0.75}$ and (e) RGO.

Figure 4.11 shows that when the concentration of RGO in the host Bi_2O_3 matrix increases, the ohmic resistance decreases. The nanocomposite $(Bi_2O_3)_{0.50}/(RGO)_{0.50}$ has a least equivalent series resistance (ESR) of 0.541 Ω. This minimum equivalent series resistance (ESR) improves the materials' electronic conductivity, which also gives the composite material used as an electrode and thus gives high specific capacitance (Cs). This minimum equivalent series resistance (ESR) enhances the electronic conductivity of materials and gives high specific capacitance (Cs) to the composite materials used as electrodes. The change in ESR values is clearly depicted in the ragone plot 4.11 with changing concentration of RGO in the host material Bi_2O_3.

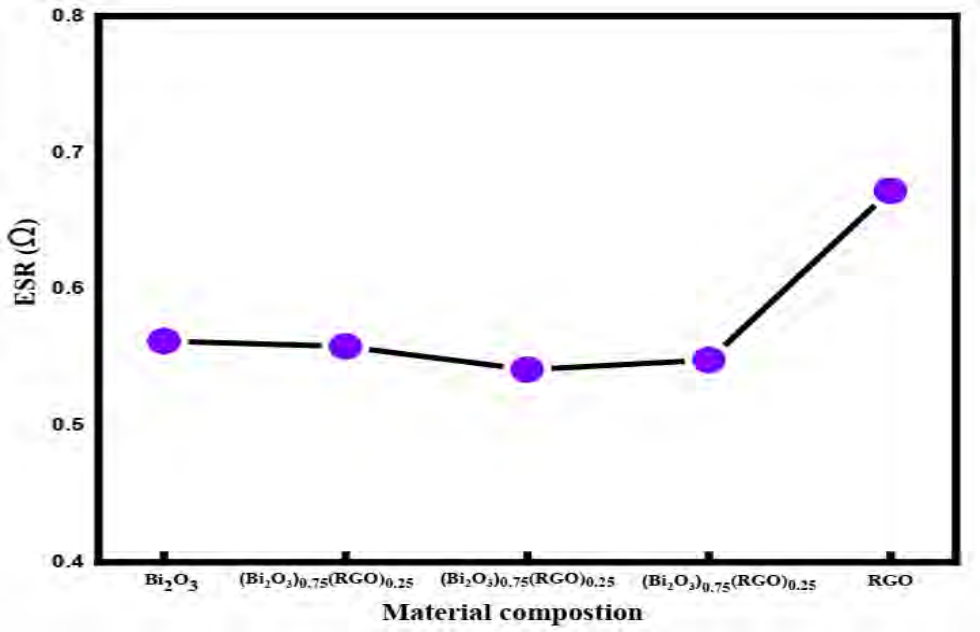

Figure 4. 6: The ragone plot for ESR with changing concentration of RGO in the host material Bi_2O_3

4.5 Cycle Stability and Coulombic Efficiency

The important characteristic of the commercial use of electrode material is its cyclic resilience. To check the reliability of the device, we put the device through continuous charge-discharge experiments for up to 1000 cycles in a six-molar KOH electrolyte. The cycling tests have been done at a current density of 2.5 Ag^{-1}. The specific capacitance retention for the $(Bi_2O_3)_{0.50}/(RGO)_{0.50}$ nanocomposite electrode is about 99% after 1000 cycles, which is much better than Bi_2O_3 and RGO, whose specific capacitance retention after the same cycles are 95% and 84%, respectively. This specific capacitance drops after multiple cycles due to the volumetric distortion of electrode materials caused by shrinkage during the reversible redox reaction [59]. However, RGO is significant in the $(Bi_2O_3)_x/(RGO)_{1-x}$ (x= 1, 0.75, 0.5, 0.25, 0) NCs because it prevents the volume distortions of the Bi_2O_3 counterpart during the redox process, enhancing the cyclic reliability. The manufactured $(Bi_2O_3)_x/(RGO)_{1-x}$ (x= 1, 0.75, 0.5, 0.25, 0) NCs is shown to have better electrochemical properties, which might be attributed to the following factors:

- The in-situ $(Bi_2O_3)_x/(RGO)_{1-x}$ (x= 0.75, 0.5, 0.25) NCs synthesis provides effective interfacial contact between Bi_2O_3 and RGO NPs.
- Rapid electron transfer and ion transport occur during the charging and discharging process due to the well-dispersed RGO's large surface area in the nanocomposite material.
- The well-dispersed RGO with a high surface area in the composite provides a high conducting pathway, resulting in fast electron transfer and ion transport during the charging and discharging process [60].
- Analysis of cycle stability data demonstrates that decreased graphene oxide enhances electrode stability. RGO's exceptional mechanical and electrical conductivity also improves structural integrity, reduces deterioration, and increases cycling effectiveness.
- This result raises the possibility that $(Bi_2O_3)_{0.50}/(RGO)_{0.50}$ exact chemical makeup was vital in improving the performance of the electrode.

The nanocomposite $(Bi_2O_3)_{0.50}/(RGO)_{0.50}$ has shown stable columbic efficiency and attained the maximum efficiency of 100%, Bi_2O_3 achieved the second-highest efficiency of 98%, and the efficiency of pure RGO is 92%. Because $(Bi_2O_3)_{0.50}/(RGO)_{0.50}$ exhibits a higher Coulombic efficiency, it is likely that the composite composition has a major impact on how effectively charge and discharge processes occur. Bismuth oxide may promote reversible redox processes in the nanocomposites, resulting in effective charge storage and utilization. The reduced graphene oxide component can operate as a conductive network to boost Columbia's efficiency and minimize unfavorable side effects. It is important to note that increasing Columbia efficiency is desirable to improve supercapacitors' overall energy storage capacity and utilization. The findings of this study show that, in comparison to the other composite electrode $(Bi_2O_3)_{0.50}/(RGO)_{0.50}$, made of 50% bismuth oxide and reduced graphene oxide, has greater cycle stability and Coulombic efficiency. These results demonstrate $(Bi_2O_3)_{0.50}/(RGO)_{0.50}$ potential for use in high-performance supercapacitors. To further enhance the overall performance of supercapacitors, future research should concentrate on refining the nanocomposite composition and examining various electrode materials.

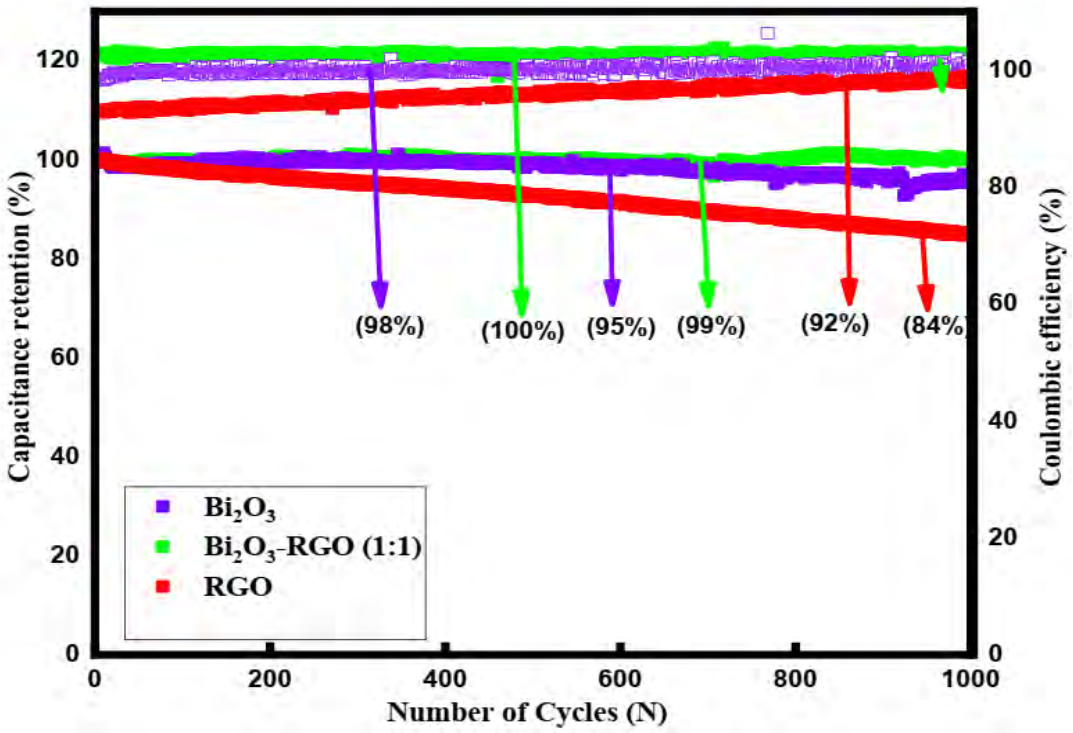

Figure 4. 7: Cycle stability and Coulombic efficiency of a Bi_2O_3, RGO and $(Bi_2O_3)_{0.50}/(RGO)_{0.50}$ NCs

Conclusions

The desired NCs $(Bi_2O_3)_x/(RGO)_{1-x}$ (x=0.75, 0.5, 0.25) with varying stoichiometric ratios have been successfully fabricated using a cost-effective and versatile ex-situ technique. The structural investigations and the vibrational spectroscopy (FTIR) have further confirmed the structure of prepared NCs. The X-ray diffraction analysis of pristine Bi_2O_3 and fabricated NCs showed slight variation in lattice parameters, decrease in crystallite size, strain dislocation and the peaks are slightly shifted towards higher angles, decreasing crystallite size and slight shift of the characteristics peaks towards higher 2θ angles which are assigned to the different concentration of RGO which have different lattice parameters as compared to the crystal structure of the host material Bi_2O_3. FTIR analysis have confirmed the bonding of $(Bi_2O_3)_x/(RGO)_{1-x}$ (x= 0.75, 0.5, 0.25) NCs and the main characteristic bands of Bi-O-Bi and Bi-O stretching vibration in pure Bi_2O_3 show a slight shift toward lower wave number in $(Bi_2O_3)_{0.50}/(RGO)_{0.50}$ NC. The bandgap energy of $(Bi_2O_3)_{0.50}/(RGO)_{0.50}$ NCs is narrowed and tuned successfully towards the visible region due to quantum confinement process and charge transfer between RGO and Bi_2O_3. The RGO is found to be act as an electron acceptor. The electrochemical studies have revealed that the synthesized samples can be effectively used as supercapacitor electrode material. Electrochemical properties of pristine Bi_2O_3 and its NCs with RGO have been performed using Cyclic Voltammetry (CV), Galvanostatic Charge Discharge (GCD), and Electrochemical Impedance Spectroscopy (EIS) at room temperature. In particular, the $(Bi_2O_3)_{0.50}/(RGO)_{0.50}$ NC maintained specific capacitance of 804 Fg^{-1} at a current density of 1 Ag^{-1} from Galvanostatic Charge discharge (GCD), 1254 Fg^{-1}, at a 5mV/s from cyclic voltammetry, and the ohmic resistance is 0.541 Ω in 6M KOH electrolyte. The symmetric supercapacitors made with these electrode materials have superior energy densities of 27.92 Wh/Kg at a power density of 900 W/Kg in comparison to the majority of previously reported symmetric supercapacitors. These electrode materials produce supercapacitors that exhibit extraordinary energy density of 27.92 Wh/Kg and a power density of 900 W/Kg, exceeding most of the symmetric supercapacitors previously reported. Remarkably, the $(Bi_2O_3)_{0.50}/(RGO)_{0.50}$ NC cyclic stability is 99%, and its coulombic efficiency approached 100%, indicating exceptional performance potential for supercapacitor applications. Further research in this direction it could lead to innovative advancements in energy storage and conversion systems.

References

[1] Kakani SL. Material science. New Age International (P) Ltd., Publishers; 2004.

[2] Poole Jr CP. FJ Owens. Introduction to Nanotechnology Wiley Intercedence, New Jersey. 2003.

[3] Ellis AB. Teaching General Chemistry: A Materials Science Companion. American Chemical Society, Distribution Office Department 225, 1155 16th Street, NW, Washington, DC 20036; 1993.

[4] Russell, A.W., Improving legitimacy in nanotechnology policy development through stakeholder and community engagement: forging new pathways. Review of policy research, 2013. 30(5): p. 566-587.

[5] Mansoori GA, Soelaiman TF. Nanotechnology--An introduction for the standards community. ASTM International; 2005 Jun 1.

[6] Jeevanandam J, Barhoum A, Chan YS, Dufresne A, Danquah MK. Review on nanoparticles and nanostructured materials: history, sources, toxicity and regulations. Beilstein journal of nanotechnology. 2018 Apr 3;9(1):1050-74.

[7] Feynman R. There's plenty of room at the bottom. Science. 1991;254:1300-1.

[8] Serrano, Elena, Guillermo Rus, and Javier Garcia-Martinez. "Nanotechnology for sustainable energy." *Renewable and Sustainable Energy Reviews* 13.9 (2009): 2373-2384.

[9] https://www.eia.gov/energyexplained/us-energy-facts

[10] Libich J, Máca J, Vondrák J, Čech O, Sedlaříková M. Supercapacitors: Properties and applications. Journal of energy storage. 2018 Jun 1;17:224-7.

[11] Koohi-Fayegh S, Rosen MA. A review of energy storage types, applications and recent developments. Journal of Energy Storage. 2020 Feb 1;27:101047.

[12] Joseph, I., et al., An Overview of the Operational Principles, Light Harvesting and Trapping Technologies, and Recent Advances of the Dye Sensitized Solar Cells. 2020. 56(5): p. 334-363.

[13] Li, M., et al., Relating catalysis between fuel cell and metal-air batteries. 2020. 2(1): p. 32-49.

[14] Zainol, M.Z., et al., Application of Contactless Inductive Charging for Ship—A Review. 2020: p. 283-298.

[15] Koohi-Fayegh S, Rosen MA. A review of energy storage types, applications and recent developments. Journal of Energy Storage. 2020 Feb 1;27:101047.
[16] Murty VV, Kumar A. RETRACTED ARTICLE: Multi-objective energy management in microgrids with hybrid energy sources and battery energy storage systems. Protection and Control of Modern Power Systems. 2020 Dec;5(1):1-20.
[17] Emmanuel O. Different types of batteries and their applications. Circuit Digest. 2018 Jul.
[18] Vangari M, Pryor T, Jiang L. Supercapacitors: review of materials and fabrication methods. Journal of energy engineering. 2013 Jun 1;139(2):72-9.
[19] Arepalli S, Fireman H, Huffman C, Moloney P, Nikolaev P, Yowell L, Kim K, Kohl PA, Higgins CD, Turano SP, Ready WJ. Carbon-nanotube-based electrochemical double-layer capacitor technologies for spaceflight applications. Jom. 2005 Dec;57:26-31.
[20] González A, Goikolea E, Barrena JA, Mysyk R. Review on supercapacitors: Technologies and materials. Renewable and sustainable energy reviews. 2016 May 1;58:1189-206.
[21] Bousmina M. Study of intercalation and exfoliation processes in polymer nanocomposites. Macromolecules. 2006 Jun 13;39(12):4259-63.

[22] Vangari M, Pryor T, Jiang L. Supercapacitors: review of materials and fabrication methods. Journal of energy engineering. 2013 Jun 1;139(2):72-9.
[23] Pereira P, Ferreira DP, Araújo JC, Ferreira A, Fangueiro R. The potential of graphene nanoplatelets in the development of smart and multifunctional ecocomposites. Polymers. 2020 Sep 24;12(10):2189.
[24] Saho E. Functionalization of Single-walled Carbon Nanotubes with Bis-astraphloxin. arXiv preprint arXiv:1907.10752. 2019 May 26.
[25] McClintock PV. Graphene: Carbon in Two Dimensions. Contemporary Physics. 2012;53(6):503-4.
[26] Haddon r, siegrist t, dabbagh g, tully j, walstedt r. Synthesis and characterization of alkali metal fullerides: axc, 0. The fullerenes. 2012 dec 2:151.
[27] Popov VN. Carbon nanotubes: properties and application. Materials Science and Engineering: R: Reports. 2004 Jan 15;43(3):61-102.

[28] Pan J, Xing H, Liu G, Wang Y, Liu X. Characterization of thermal properties of bituminous mastic containing different fillers to be used in the cool pavement. Construction and Building Materials. 2020 Dec 30;265:120362.

[29] Sasa T, Takahashi Y, Mukaibo T. Crystal structure of graphite bromine lamellar compounds. Carbon. 1971 Aug 1;9(4):407-16.

[30] Mitra S, Sampath S. Electrochemical capacitors based on exfoliated graphite electrodes. Electrochemical and solid-state letters. 2004 Jul 23;7(9):A264.

[31] Naseri M, Jalilian J, Salahub DR, Lourenço MP, Rezaei G. Hexatetra-Carbon: A Novel Two-Dimensional Semiconductor Allotrope of Carbon. Computation. 2022 Jan 25;10(2):19.

[32] Pisana S, Lazzeri M, Casiraghi C, Novoselov KS, Geim AK, Ferrari AC, Mauri F. Breakdown of the adiabatic Born–Oppenheimer approximation in graphene. Nature materials. 2007 Mar;6(3):198-201.

[33] Yang G, Li L, Lee WB, Ng MC. Structure of graphene and its disorders: a review. Science and technology of advanced materials. 2018 Dec 31;19(1):613-48.

[34] Choi W, Lahiri I, Seelaboyina R, Kang YS. Synthesis of graphene and its applications: a review. Critical Reviews in Solid State and Materials Sciences. 2010 Feb 11;35(1):52-71.

[35] Avouris P, Dimitrakopoulos C. Graphene: synthesis and applications. Materials today. 2012 Mar 1;15(3):86-97.

[36] Balasooriya ER, Jayasinghe CD, Jayawardena UA, Ruwanthika RW, Mendis de Silva R, Udagama PV. Honey mediated green synthesis of nanoparticles: new era of safe nanotechnology. Journal of Nanomaterials. 2017 Mar 5;2017.

[37]Fernández-Arias M, Vilas AM, Boutinguiza M, Rodríguez D, Arias-González F, Pou-Álvarez P, Riveiro A, Gil J, Pou J. Palladium nanoparticles synthesized by laser ablation in liquids for antimicrobial applications. Nanomaterials. 2022 Jul 29;12(15):2621.

[38]Sood S, Umar A, Mehta SK, Kansal SK. α-Bi2O3 nanorods: An efficient sunlight active photocatalyst for degradation of Rhodamine B and 2, 4, 6-trichlorophenol. Ceramics International. 2015 Apr 1;41(3):3355-64.

[39] Alam SN, Sharma N, Kumar L. Synthesis of graphene oxide (GO) by modified hummers method and its thermal reduction to obtain reduced graphene oxide (rGO). Graphene. 2017 Jan 10;6(1):1-8.

[40] Sam, Z., et al., Materials Characterization Techniques. 2009. 7: p. 177-205.

[41] Leng Y. Materials characterization: introduction to microscopic and spectroscopic methods. John Wiley & Sons; 2009 Mar 4.

[42] Zhang S, Li L, Kumar A. Materials characterization techniques. CRC press; 2008 Dec 22.

[43] Weiss Z, Wyslych P, Capkova P, Kristkova M, Havlova D. Analysis of Nanostructured Materials Ph D Course. International Journal of Engineering Education. 2002;18(5):532-8.

[44] Baskaran S. *Structure and regulation of yeast glycogen synthase* (Doctoral dissertation).

[45] Singh AK. Advanced x-ray techniques in research and industry. IOS press; 2005.

[46] Tu Q, Chang C. Diagnostic applications of Raman spectroscopy. Nanomedicine: Nanotechnology, Biology and Medicine. 2012 Jul 1;8(5):545-58.

[47] Braga MS, Gomes OF, Jaimes RF, Braga ER, Borysow W, Salcedo WJ. Multispectral colorimetric portable system for detecting metal ions in liquid media. In2019 4th International Symposium on Instrumentation Systems, Circuits and Transducers (INSCIT) 2019 Aug 26 (pp. 1-6). IEEE.

[48]Rocha FS, Gomes AJ, Lunardi CN, Kaliaguine S, Patience GS. Experimental methods in chemical engineering: Ultraviolet visible spectroscopy—UV-Vis. The Canadian Journal of Chemical Engineering. 2018 Dec;96(12):2512-7.

[49] Akhtar K, Khan SA, Khan SB, Asiri AM. Scanning electron microscopy: Principle and applications in nanomaterials characterization. Handbook of materials characterization. 2018:113-45.

[50] Wang G, Zhang L, Zhang J. A review of electrode materials for electrochemical supercapacitors. Chemical Society Reviews. 2012;41(2):797-828.

[51]Ramadoss A, Kim SJ. Improved activity of a graphene–TiO2 hybrid electrode in an electrochemical supercapacitor. Carbon. 2013 Nov 1;63:434-45.

[52] Ferreira Jr JM, Souza KP, Queiroz FM, Costa I, Tomachuk CR. Electrochemical and chemical characterization of electrodeposited zinc surface exposed to new surface treatments. Surface and Coatings Technology. 2016 May 25;294:36-46.

[53] Sood S, Umar A, Mehta SK, Kansal SK. α-Bi2O3 nanorods: An efficient sunlight active photocatalyst for degradation of Rhodamine B and 2, 4, 6-trichlorophenol. Ceramics International. 2015 Apr 1;41(3):3355-64.

[54] Devi NA, Sinha S, Nongthombam S, Swain BP. Structural, optical, electrochemical and electrical studies of Bi2O3@ rGO nanocomposite. Materials Science in Semiconductor Processing. 2022 Jan 1;137:106212.

[55] Sharma N, Sharma V, Jain Y, Kumari M, Gupta R, Sharma SK, Sachdev K. Synthesis and characterization of graphene oxide (GO) and reduced graphene oxide (rGO) for gas sensing application. InMacromolecular Symposia 2017 Dec (Vol. 376, No. 1, p. 1700006).

[56] Gurusamy L, Anandan S, Liu N, Wu JJ. Synthesis of a novel hybrid anode nanoarchitecture of Bi2O3/porous-RGO nanosheets for high-performance asymmetric supercapacitor. Journal of Electroanalytical Chemistry. 2020 Jan 1;856:113489.

[57] Maruthamani D, Vadivel S, Kumaravel M, Saravanakumar B, Paul B, Dhar SS, Habibi-Yangjeh A, Manikandan A, Ramadoss G. Fine cutting edge shaped Bi2O3rods/reduced graphene oxide (RGO) composite for supercapacitor and visible-light photocatalytic applications. Journal of colloid and interface science. 2017 Jul 15;498:449-59.

[58] Ramya R, Sivasubramanian R, Sangaranarayanan MV. Conducting polymers-based electrochemical supercapacitors—progress and prospects. Electrochimica Acta. 2013 Jul 1;101:109-29.

[59] Nagamuthu S, Vijayakumar S, Muralidharan G. Ag incorporated Mn 3 O 4/AC nanocomposite-based supercapacitor devices with high energy density and power density. Dalton Transactions. 2014;43(46):17528-38.

[60] Vijayakumar S, Nagamuthu S, Muralidharan G. Porous NiO/C nanocomposites as electrode material for electrochemical supercapacitors. ACS Sustainable Chemistry & Engineering. 2013 Sep 3;1(9):1110-8.